THERMO-MECHANICAL MODELLING FOR WIRE ARC

ADDITIVE MANUFACTURING

submitted in partial fulfillment of the requirements
for the degree of

BACHELOR OF TECHNOLOGY
in
MECHANICAL ENGINEERING
by

MOHAMMED SALEEQ K	**ME18B016**
NATESH ARAVIND S	**ME18B018**
VIJAY KUMAR THOKALA	**ME18B034**

Supervisor(s)

Dr. D. V. Kiran

भारतीय प्रौद्योगिकी संस्थान तिरुपति

IIT

T I R U P A T I

DEPARTMENT OF MECHANICAL ENGINEERING

INDIAN INSTITUTE OF TECHNOLOGY

MAY 2022

DECLARATION

We declare that this written submission represents our ideas in our own words and where others' ideas or words have been included, we have adequately cited and referenced the original sources. We also declare that we have adhered to all principles of academic honesty and integrity and have not misrepresented or fabricated or falsified any idea/data/fact/source in our submission to the best of our knowledge. We understand that any violation of the above will be cause for disciplinary action by the Institute and can also evoke penal action from the sources which have thus not been properly cited or from whom proper permission has not been taken when needed.

Place: Tirupati

Date: 25-05-2022

Mohammed Saleeq K

ME18B016

Natesh Aravind S

ME18B018

Vijay Kumar Thokala

ME18B034

BONA FIDE CERTIFICATE

This is to certify that the report titled **THERMO-MECHANICAL MODELLING FOR WIRE ARC ADDITIVE MANUFACTURING**, submitted by **Mohammed Saleeq K, Natesh Aravind S,** and **Vijay Kumar Thokala** to the Indian Institute of Technology, Tirupati, for the award of the degree of Bachelor of Technology, is a bona fide record of the research work done by them under my supervision. The contents of this thesis, in full or in parts, have not been submitted to any other Institute or University for the award of any degree or diploma.

D.V. Kiran

Place: Tirupati

Date: 25-05-2022

Dr. D. V. Kiran

Guide

Assistant Professor

Department of

Mechanical Engineering

IIT Tirupati - 517619

ACKNOWLEDGEMENTS

ABSTRACT

Metal additive manufacturing has the potential to revolutionize the aerospace, automobile and energy industries which require large and complex parts. Wire arc additive manufacturing is one such process that has grabbed industry attention as existing GMAW robots can easily be adopted for the WAAM process. But the mechanical properties of these components are inferior compared to the conventionally manufactured components due to the complex thermal cycles involved. As experimentally determining the optimal process parameters are extremely resource and cost intensive the best alternate is to rely on simulation of the process. This research work focuses on developing a modified heat source model to account for the arc elongation phenomena and an analytical model to estimate the thermal cycles and predict the metallurgical properties of the final part quickly and efficiently.

Key Words: WAAM, Heat source modelling, Analytical modelling

TABLEOF CONTENTS

LIST OF FIGURES

LIST OF TABLES

CHAPTER 1

INTRODUCTION

Wire arc additive manufacturing (WAAM) is a type of Directed Energy Deposition (DED) process developed based on the Gas Metal Arc Welding (GMAW) technology. When compared to the other DED processes, WAAM has the highest deposition rate which is advantageous for manufacturing large and complex structural components. Adding to this since WAAM setup is basically a modified GMAW setup, no special machinery is required, and the setup can be scaled-up to build structures of any size. However, the major downside with this technology is the non-uniformity in the microstructure of the manufactured components.

Due to the inherent nature of the layer-by-layer deposition, the previously deposited layers gets reheated and cooled multiple times results in a variation of microstructural and metallurgical properties within each layer. Therefore, to control the microstructure of the manufactured part proper process parameters have to be decided. Experimentally determining these parameters is very resource intensive and costly endeavor which is generally not favored and instead simulations are used to predict the time-temperature data of the WAAM process which can be further correlated with the metallurgical properties of the final part.

While there have been past efforts in simulating the WAAM process using numerical models and analytical models, most of the models themselves either require huge computational time or only model localized regions of the part. Both of which are not suitable when it comes to simulating large components. *Therefore, our work majorly focuses on simultaneously developing a numerical and analytical model that can quickly and efficiently predict the thermal cycles and metallurgy.*

CHAPTER 2

LITERATURE SURVEY

2.1 Numerical Modelling

Throughout the years numerous finite element methods have been developed by various researchers to model the process of wire arc additive manufacturing, with many of the recent works focusing on Multiphysics 3D models with complex considerations like- Hu and Tsai et al. (2007) whose model considered the simulation of molten metal flow, convective currents in the weld pool and arc physics. Ding et al (2011) and Xingwang Bai et al. (2018) in their modelling of plasma arc welding (PAW) based WAAM process showed how the fluid motion is significantly affected by the Marongani effect. Cadiou et al. (2020) even considered electromagnetism and fluid flow to incorporate the complex droplet formation and detachment mechanisms involved in cold metal transfer (CMT) welding process. But almost all such 3D Multiphysics models restrict their domain of simulation within the vicinity of the weld pool and fail to incorporate the complete model to reduce the computational duration. While being extremely accurate within the domain, the resource intensive nature of these simulation requires huge computational time [Montevecchi et al. (2016)] and cost investment, which in addition to the localized nature of the study, renders it infeasible when considering simulation of large-scale parts.

Therefore, In the recent years there has been a shift of focus towards computationally simpler Finite Element Method based thermo-mechanical models. Such as the ones reported by Marcel Graf et.al (Metals 2018) where they compared the thermal cycle data obtained from their model, with the experimental data collected using thermocouples and observed correlation with slight deviations due to some of the

underlying assumptions in their model. AVSK Chaitanya et al. (BTP 2021) were partially successful in decreasing the deviations observed in Marcel Graf's work by considering a surface heat flux model with gaussian distribution [Kiran et al. (2016)] instead of the double ellipsoidal volumetric heat source model [Goldak et al. (1984)] used by Graf, that ignores the power distribution between filler and base metal in the GMAW based WAAM process.

But the main drawback with both heat sources models mentioned above is that they were originally developed for welding processes and do not consider the effect of arc elongation that occurs during multi-layer deposition. Xingwang Bai et al. (2018) had developed a modified double ellipsoidal volumetric heat source for their multi-physics simulation of PAW based WAAM process. While their CFD model was able to predict the overall component shape to some extent not much was reported about the thermal cycles and metallurgy. *Therefore, there is a need to develop a modified surface heat flux model that can be used for coupled thermo-mechanical models, that incorporates this arc elongation phenomenon and the consequential reheating of the previously deposited layers.*

The arc elongation phenomenon has a significant impact on determining the metallurgical properties of parts manufactured using WAAM. *As accurate time-temperature data is needed to predict and control the phase changes within the layers and could also prove quintessential in avoiding delamination failure of the deposited layers during the WAAM process.* Additionally, Xingwang Bai et al. (2018) and AVSK Chaitanya et al. (BTP 2021) also noted from their experiments that the dominant mode of heat transfer is via conduction within the part and to the weld table as compared to heat dissipation by convection and radiation to air. However, accurate modeling of heat transfer to the weld table has generally been ignored in most of the existing literature work potentially leading to the deviations in the thermal cycles observed in the works by Marcel Graf et.al (Metals 2018) and AVSK Chaitanya et al. (BTP 2021).

2.2 Analytical Modelling

As seen in the previous sub-section 1.1, thermo-mechanical modelling for wire arc additive manufacturing process has been done by various researchers over the years focusing on various applications. However, all of these works primarily use finite element analysis (FEA) which is heavily time and resource intensive. Contrary to this, faster analytical modelling approaches have already been developed for multi-pass welding, a process which has close similarities with the process conditions of WAAM.

Carslaw et al. (1967) published a mathematical heat transfer model using instantaneous point heat sources to predict the time-temperature correlation. Further N.T Nguyen et al. (2004) extended Carslaw's work for Goldak et.al (1984)'s volumetric double ellipsoidal heat source and obtained the thermal cycles for single pass welding. A more detailed attempt at modeling the thermal cycles for multi-pass welding was done by R.N.S Fassani et.al. (2003). However, R.N.S Fassani's work uses a pavelic-disc heat source model which is known to be less accurate [Goldak et.al (1984)]. But none of the above work include prediction of metallurgical characterization of the welds. R.C Reed et.al (1994) did exemplary work in predicting metallurgical characteristics of multi-pass welds using the thermal cycles obtained but his work was based on numerical modelling of the process and not analytical which is extremely resource intensive.

The analytical model thus presented combines the analytical models developed by N.T Nguyen and later modified by V.D Fachinotti, to correct the mathematical simplifications. With the metallurgical analysis done by R.C Reed, and further scope for optimizing the model is explored. The analytical model was also utilized to estimate double ellipsoidal heat source parameters for numerical simulations using the same heat source, following the reference from Chujutalli et.al. *This will be extremely useful in deciding various critical parameter for the WAAM process such as: pre-heating temperature, inter-pass temperature, inter-pass time and scanning strategies.*

CHAPTER 3

NUMERICAL MODELLING

3.1   Problem Formulation

To simulate the WAAM process, a three-dimensional transient heat conduction analysis is carried out with the governing equation given by:

$$\frac{\partial}{\partial x}\left(k\frac{\partial T}{\partial x}\right) + \frac{\partial}{\partial y}\left(k\frac{\partial T}{\partial y}\right) + \frac{\partial}{\partial z}\left(k\frac{\partial T}{\partial z}\right) + \dot{Q} = \rho C \frac{\partial T}{\partial t} \qquad (3.1)$$

In the equation. (3.1), k, ρ and C refer to thermal conductivity, density, and specific heat respectively while T and t are temperature and time variables respectively. $\dot{Q}$ is the rate of internal heat generation per unit volume. The boundary conditions can be given by the equation:

$$k_n\frac{dT}{dn} - q_s + h(T - T_0) + \sigma\varepsilon(T^4 - T_0^4) = 0 \qquad (3.2)$$

In the equation. (3.2), *kn* refers to thermal conductivity, where n is the direction normal to surface. h is the convective heat transfer coefficient on the surface and it was taken as h = 10 W/m2K as suggested by Tekriwal et al. (1988) in the initial simulation. σ is the Stephen-Boltzmann constant which is given by σ = 5.67 x 10-8, whereas ε is the emissivity of the material which is assumed to be 0.83. The first term in the left-hand side of the equation. (3.2) accounts for the conduction heat losses from the surface who's normal is given by n. The third and fourth terms in corresponds to the convection and radiation heat losses from the surface exposed to the air. *qs*, the second term, accounts for the arc heat input which is estimated using a Gaussian surface heat flux. This heat source model is explained in detail in Section: 3.2. There is a significant amount of heat transfer from the bottom surface of the base plate to the weld table due to conduction. Without the weld table in the analysis, this conduction heat loss cannot

be incorporated directly. To account for this, an overall heat transfer coefficient of 200W/m^{2}K is assigned for the bottom surface of the base plate, which governs the rate of heat loss to the weld table from the base plate. This value is estimated by iterating the numerical analysis until the temperature profiles measured from the numerical model reasonably agree with the experimental temperature profiles obtained by Chaitanya et. al. (BTP 21-22). As the base plate is not preheated before the experiments, the initial temperature of the base plate (as well as the ambient temperature T0) is assumed as 300 K (room temperature). In order to incorporate the effect of molten metal deposition in the current analysis, the element deactivation and reactivation technique followed by Kiran et al. (2016) is used. Using this technique, the bead elements are reactivated at a temperature of 2300 K. As an inter-pass temperature of 150 C is maintained while performing the experiments, the same has been incorporated in the current analysis.

3.2   Heat Source Model

Each CMT cycle consists of 3 phases: Peak current phase, background current phase, and short-circuiting phase. During the first two phases of the CMT cycle, the welding arc is active. In the GMAW technology used for the WAAM process, the arc power is transferred to the molten pool in two ways: direct energy transfer to the base metal from electric arc and indirect energy transfer through droplets enthalpy, which is used for melting of filler metal [Montevecchi et al. (2016)]. To take this power distribution into account, a surface heat flux model with Gaussian distribution [Kiran et al. (2016)] is adopted for direct energy transfer from the electric arc.

For simple bead on plate deposition with very low weld speeds we can consider momentarily stationary gaussian heat source, where the forward and the rear arc root radii can be considered equal. i.e., $R_R = R_F = R$. Equation (3.3) represents the arc heat input considered as a surface heat flux with Gaussian distribution:

$$q_s = \frac{\beta \eta VI}{2\pi R^2} \exp\left[-\frac{1}{2}\left(\frac{x^2}{R^2} + \frac{(z-z_i)^2}{R^2}\right)\right] \qquad (3.3)$$

Where z_i is the z coordinate of arc center in welding direction; the terms V and I represents the instantaneous welding voltage and current respectively; β refers to the fraction of the available energy utilized in melting the base plate by the arc, calculated using the method described in [Kiran et al. (2016)]; η is the efficiency of the heat source. 'V' & 'I' are calculated using regression models from experimental readings.

In the short-circuiting phase — as the arc extinguishes — the heat input is due to the resistance heating of the molten wire. During this phase, the heat input equation is borrowed from the work of Hermans and Den Ouden (1998) and is given by:

$$q_{ss} = \frac{\rho_r L_s I_s^2}{(\pi R_w^2)(\pi R_p^2)} \qquad (3.4)$$

In the equation (3.4), qss refers to the surface heat flux during the short-circuiting phase. ρr refers to the electrical resistivity of the welding wire. It is taken as 15x10-7Ω-m. Ls is the electrode extension during the short-circuiting phase. Is refers to the average short-circuiting current. Rw and Rp denotes the radius of the welding wire and projected radius of the welding droplet, respectively. The values of Ls, Rw and Rp are taken as 12mm, 0.6mm and 0.7mm respectively, in the present analysis.

3.3   Modified Boundary Conditions

The initial simulation done based on the parameter decided by [Chaitanya et al. (BTP 2021)] has significant deviations when compared to experimental data as observed in Figure 3.2 (Discussed in detail in Section 5.1). This deviation is caused due to the assumption that the weld table acts as a heat sink and was modelled with a constant h value [Chaitanya et al. (BTP 2021)]. But in reality, initially when the weld table is cool, due to the high temperature difference, the rate of heat transfer to the

weld table is extremely high and this reflects in the steeper cooling rates and the lower valley points. But as further layers get deposited, the weld table gets heated up and the rate of heat transfer to the weld table slowly decreases, which is observed as slower cooling rates and higher valley points in the experimental data.
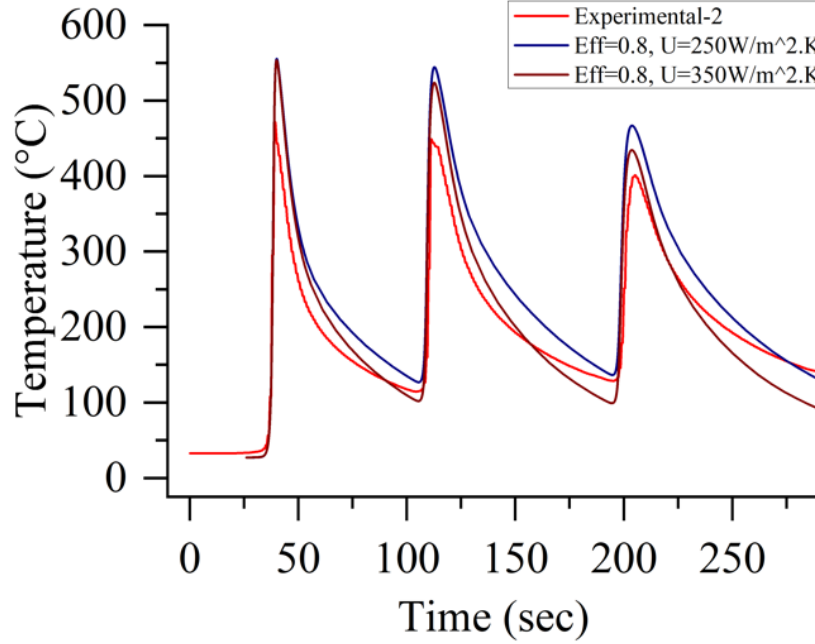
[Figure 3.1: Comparison of numerical results with experimental data]

Another assumption that was considered is that the convective heat transfer coefficient was taken to be a constant value for all surfaces which resulted in almost linear cooling curves in the prediction, but in reality, we can observe that with decrease in temperature the cooling rates also decrease. To tackle the above-mentioned issues the convective heat loss terms considered in the simulations are being varied with change in temperature of the nodes. For this purpose, a combined heat transfer coefficient [equation (3.5)] for convection and radiation, calculated by Goldak is used.

$$h = 2.4 \times 10^{-3} \times \varepsilon \times T^{1.61} \; 1.61 \; Wm^{-2}K^{-1} \qquad (3.5)$$

Where h represents the combined heat transfer coefficient, ε represents the emissivity term and T represents the nodal temperature.

3.4   Deviations Observed in the Arc

For a simple bead on plate deposition, the arc interacts only with a flat base plate, therefore the gaussian distribution assumption holds true for the distribution of the total heat input from the arc. But in case of additive manufacturing where multiple stacked bead-on-bead depositions are involved the heat distribution is no longer a simple gaussian distribution spread across the x-axis (Figure 1C), but a part of the heat input goes into reheating the side walls of the previously deposited layers as observed in our experiments. This phenomenon is referred to as arc elongation.

[Figure 3.2: Shows the comparison between high-speed images of the arc for: A. (left) single bead on plate deposition; B. (center) bead on bead deposition at a height; C. (right) Illustrates the arc elongation phenomenon.]

Figure-1 B & C clearly illustrate the arc elongation phenomenon along the side walls for a certain depth before it splits and widens midway resulting in an uneven reheating of the sidewalls. As a result of the only until a certain depth the side walls get preheated whereas the layers below that don't. *This leads to localized residual stress buildup during the deposition process and if left unaccounted could result in delamination failure of the previously deposited layers.*

3.5 Experiment to Capture Arc Elongation
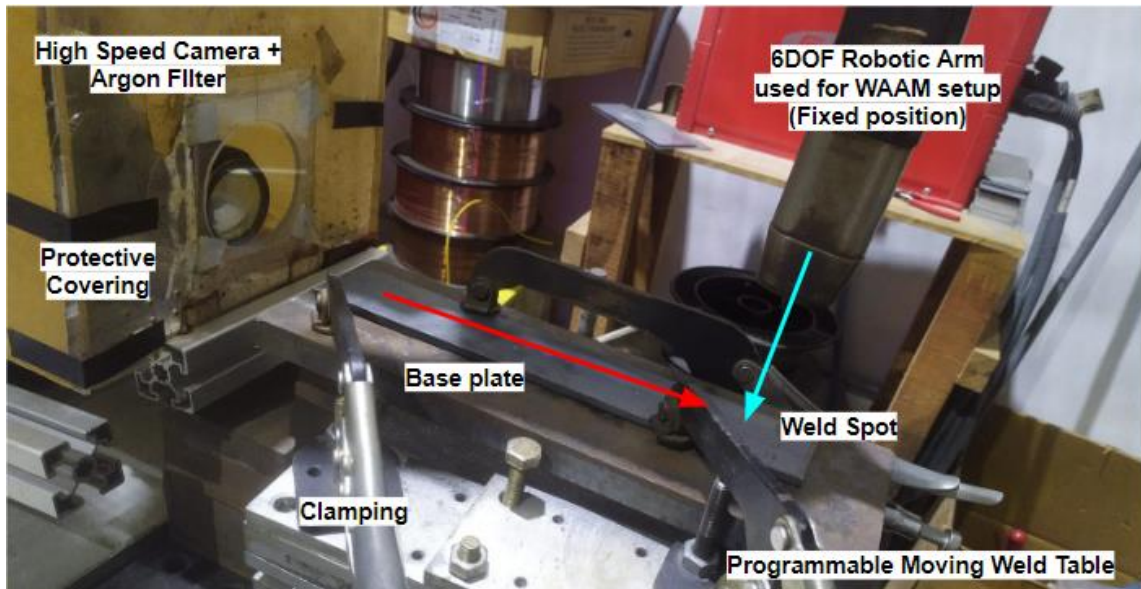
[Figure 3.3: The Modified CMT GMAW setup used to capture the arc elongation phenomenon. The figure also shows the various essential components of the setup]

The setup shown above in Figure 3.3 has been used to capture the arc elongation data for precise modelling of the same. The experimental setup is that of a modified CMT (Cold Metal Transfer) based GMAW setup for WAAM application. The 6 DOF robotic arm and the moving weld table were programmed accordingly to deposit 7 layers with a Wire Feed Rate (WFR) of 2.2 m/min and a Travel Speed of 4 mm/sec. The arc is captured using a High-Speed Camera attached with an Argon filter to later convert the intensity readings to Temperature readings. Thought the experiment the following shutter speed were tested with: 200K, 100K, 50K, 20K, 6.4K and 3K.

[Figure 3.4: The final sample after 7-layer deposition for 4 different shutter speeds]

For each layer the arc images were captures at 4 different shutter speeds to completely capture the arc details as a few details will be lost in supersaturation and under saturation of pixel data. Figure 3.6 shows the images captured at 3K and 200K shutter speeds for the 7th layer deposition, where we can observe that the central arc is clearly captured in 200K shutter speed whereas it is completely supersaturated and the arc elongation is clearly captured in the 7K shutter speed images.
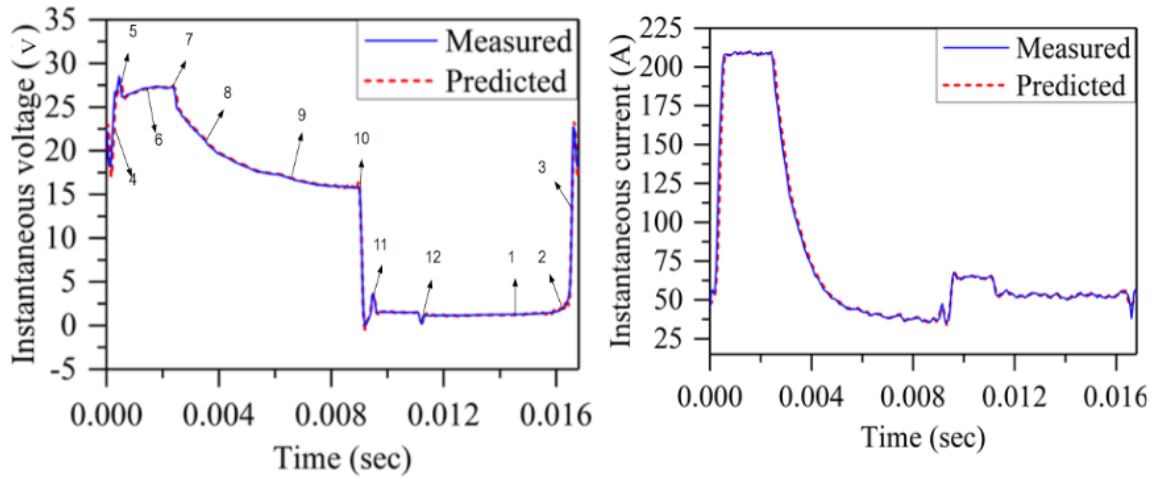
[Figure 3.5: The plots show the Voltage waveform used and the Current waveform used for the experiment. Marked along the points are the images time instances for which the arc images are shown in Figure 3.6]
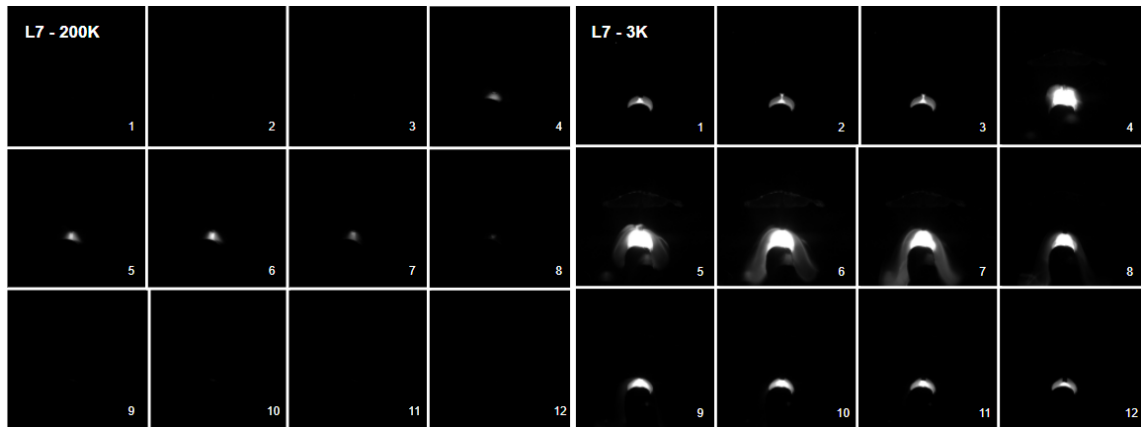
[Figure 3.6: Arc images captured at 200K and 7K shutter speeds for the 7th layer deposition at the time instances marked in Figure 3.5]

3.6   Image Processing – Intensity Prediction

As discussed in the previous section [Section 3.2] different shutter speeds expose

different temperature ranges and thus different regions of the arc. To obtain one single image to represent all the details the captured images are combined using image processing. The following steps are followed as a part of image processing done using the python code developed:

[Figure 3.7: The image shows the various intermediate steps followed in image processing to get combined image. The green regions represent the 200K shutter speed image data and red region represents the 3K shutter speed image data]

Firstly, the two images with the most extreme ranges are selected, this is generally done by selecting the maximum and the minimum shutter speeds captured given these 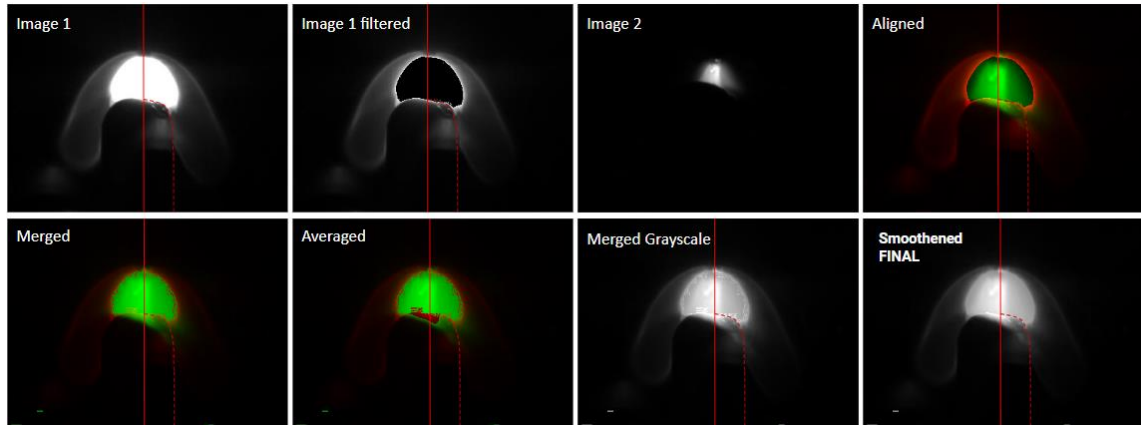to images cover the entire temperature range. Secondly, all the super saturated images (especially in the central arc zone) are removed and the two images are scaled up aligned with the welding electrode as the reference point for alignment. Next the intensities of the images are scaled to map them to different ranges of the final image to achieve the continuous capturing of all the details in a single image.

Finally, a threshold is set to avoid the background noise from upscaling and to further achieve a smoother transition between different maps especially in the overlapping zones, the average intensities are calculated and supersaturation is completely removed by further tweaking of the averaging threshold. Once the combined image is generated, the python code developed has a GUI to map the contour of the side wall using linear (for side wall) and elliptical approximation (for the bead), along which the pixel intensity data is captured and recorded. Figure 3.8 below

shows the data captured for one of the images of the 7th layer deposition along with the GUI developed to map the contour.
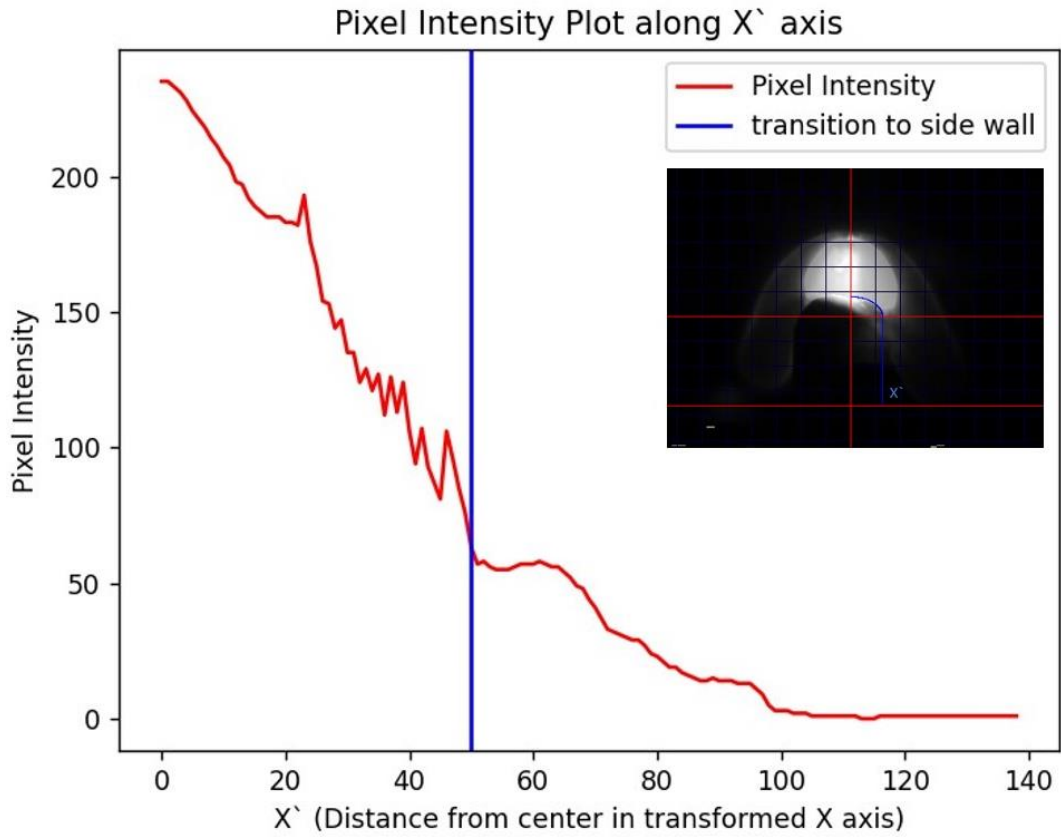
[Figure 3.8: Plot of the Pixel Intensity vs Pixel Distance data obtained for the 7th layer deposition. The top right corner shows the GUI developed to map the contour.]

3.7   Temperature Distribution Prediction

The captured pixel intensity data is then normalized to get the irradiance data along the contour. This can relation can be shown by the following derivation: Let us assume $\varepsilon(x,z)$ represent the actual irradiance values (range: 0 to 1) and I(x) represent the pixel intensity as observed in the image. Assuming that all light emitted in line of sight of a pixel is received at the end, we can formulate that,

$$I(x) = \int_{-\infty}^{\infty} \varepsilon(x,z)dz \qquad (1)$$

For practical approximation the limits are changed, where a represents the critical distance large enough to capture any measurable irradiance.

$$I(x) = \int_{-a}^{a} \varepsilon(z, x)dz \tag{2}$$

Since $\varepsilon(z, x)$ is nothing but a 2D distribution function representing how the total intensity I(x) is distributed along the z axis, it can be written as product of 2 distributions along x and z,

$$I(x) = \int_{-a}^{a} s. D_z(z). D_x(x, z)dz \tag{3}$$

Where, 's' is the scaling factor which makes sure I(x) ranges between 0 to 1. And, $D_z(z)$ and $D_x(x, z)$ represent the intensity distribution functions along z and x respectively. They are any arbitrary functions with $\int_{-a}^{a} D_z(z)dz$ and $\int_{-a}^{a} D_x(x, z)dz = 1$ (Probability Distribution Functions). By applying integration by parts in the above equation we get,

$$I(x) = s \left[D_x(x, z) \int_{-a}^{a} D_z(z)dz - \int_{-a}^{a} \left(\frac{\partial D_x(x, z)}{\partial z} . \int_{-a}^{a} D_z(z)dz \right) dz \right] \tag{4}$$

Due to the symmetry of the distribution function w.r.t center, $[D_z(z)]_{-a}^{a}$ and $[D_x(x, z)]_{-a}^{a} = 0$, and $\int_{-a}^{a} D_z(z)dz$ and $\int_{-a}^{a} D_x(z, x)dz = 1$ based on how they were defined in equation 4.

$$\Rightarrow I(x) = s. D_x(z, x) - s. \int_{-a}^{a} \frac{\partial D_x(x, z)}{\partial z} dz = s. D_x(z, x) - s. [D_x(x, z)]_{-a}^{a} \tag{5}$$

$$\Rightarrow I(x) = s. \boldsymbol{D_x(z, x)} \tag{6}$$

Therefore, we can observe that the irradiance distribution $\boldsymbol{D_x(z, x)}$ is just a

24

normalized representation of I(x), with s acting as the scaling factor for normalization. This normalized pixel intensity data (irradiance) is subsequently converted to temperature vs distance data using Fowler-Milne method as described in Vilarinho et. al. (2003). This method is used to convert the irradiance data to temperature data based on the Argon emission lines that are observed in its spectroscopic analysis. Spectroscopic experiments were also carried out to confirm that the maximum of arc intensity as observed through the Argon filter is of Argon Emission line. After conversion the data is again normalized and then fitted with an appropriate gaussian distribution to model the temperature variation along the surface.
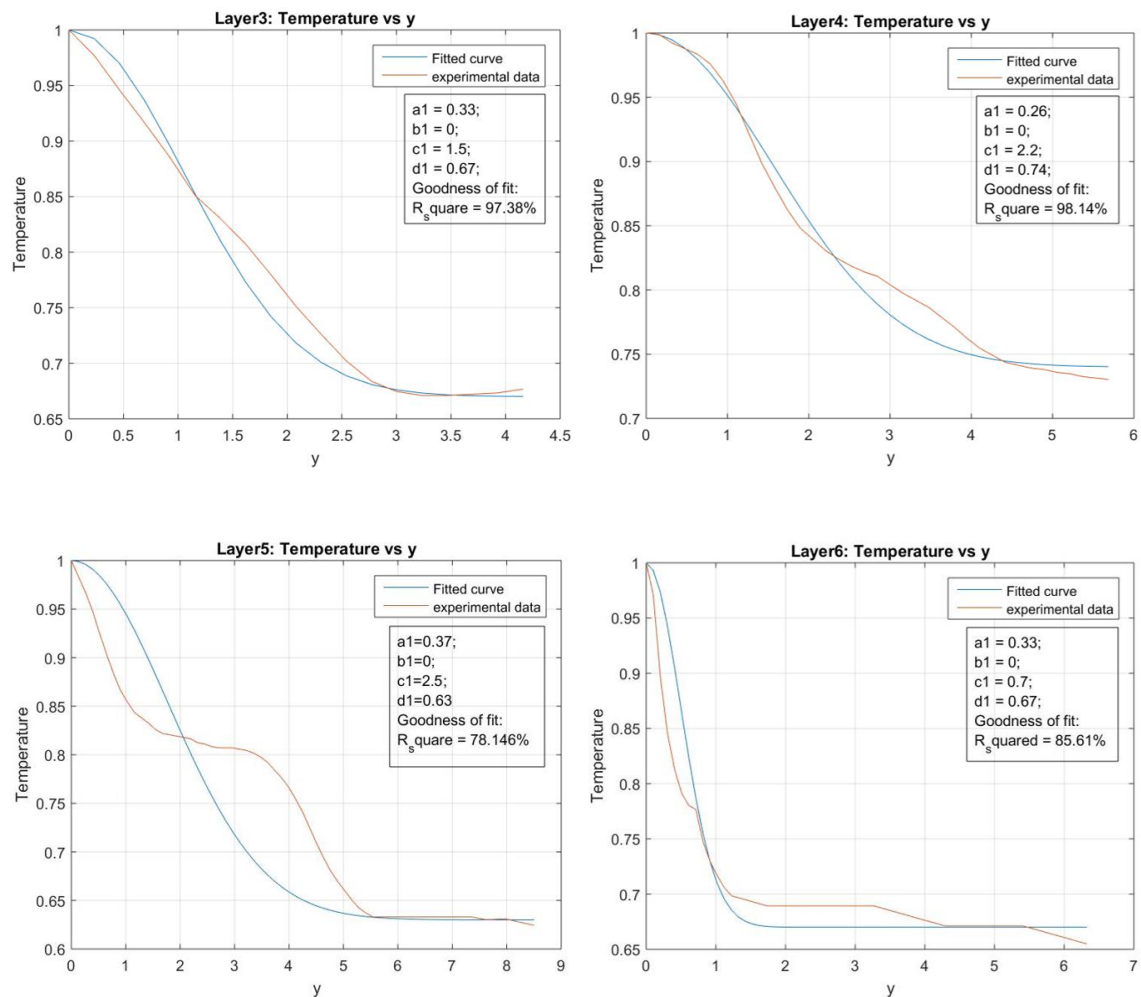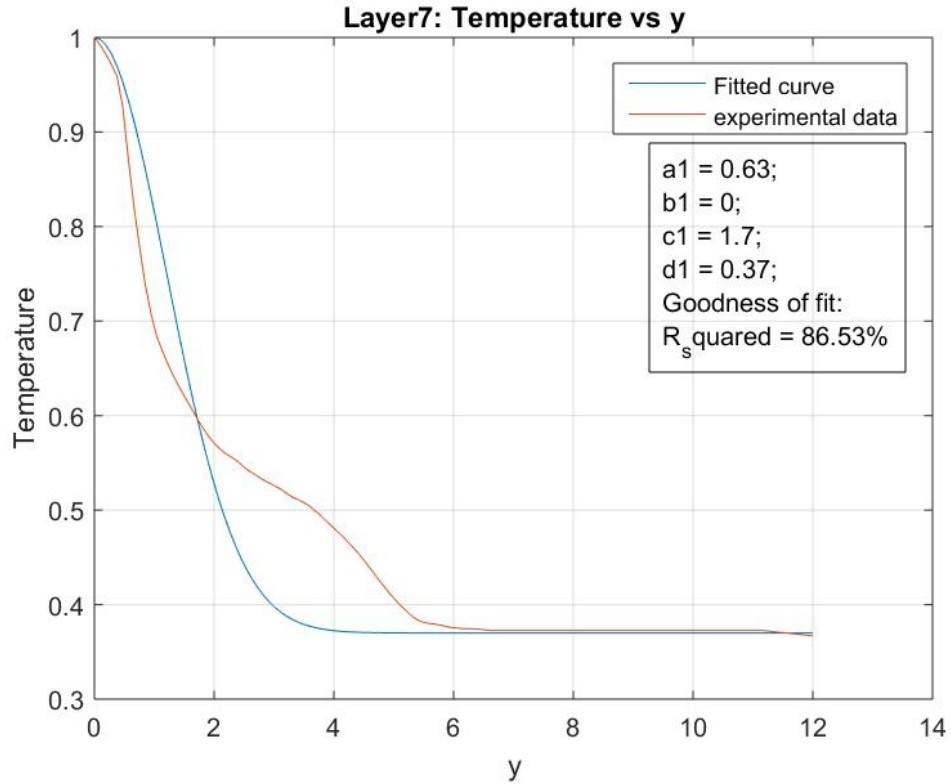
[Figure 3.9: Shows the normalized temperature data vs actual distance along the contour and the gaussian model curve fitted against it for Layers 3 to 7. The parameters of the gaussian equation fitted and the r-squared value for goodness of fit is also given below the legend for each plot]

The data obtained after fit as shown in Figure 3.9 is the Temperature distribution along the side wall only. Since the arc elongation phenomenon is observed only in the side walls the same R (Arc root radios) value for the gaussian equation is utilized for the bead surface. This data represented as $T(x')$ is used to obtain the final heat flux distribution equation $q_s(z, x)$.
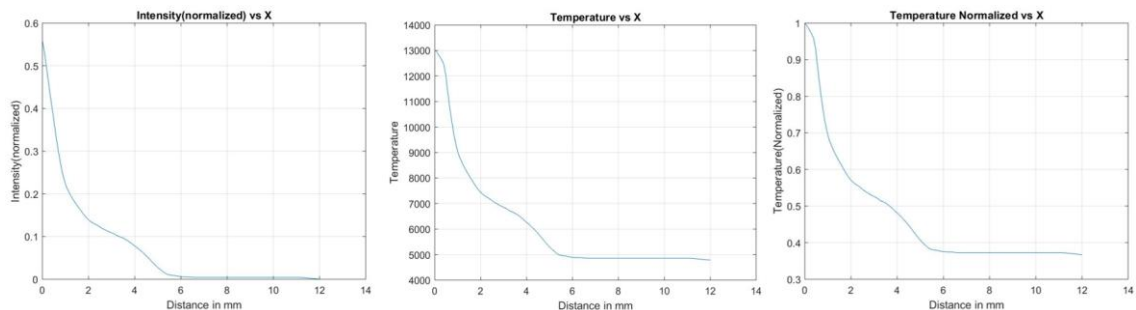
[Figure 3.10: Shows the intensity normalized, temperature and temperature normalized data as obtained using Fowler-Milne transformations]

3.8   Modification of the Gaussian Heat Source

$$q_s(x,z) = (\frac{\beta\eta VI}{\sqrt{2\pi}R}\exp{[-\frac{1}{2}(\frac{z-z_i}{R})^2]})(\frac{1}{\sqrt{2\pi}R}\exp{\left[-\frac{1}{2}(\frac{x}{R})^2\right]}) \qquad (8)$$

The gaussian heat flux distribution $q_s(x,z)$ at any point in the xz-plane is given by the equation (8) which is decomposed into 2 terms namely $q_z(z)$ and $q_x(x)$. *Where $q_z(z)$ is the gaussian coefficient of $q_s(x,z)$ which represents the total heat flux input at a given position in z-axis integrated over the x-axis*, and the $q_d(x)$ term is the gaussian distributor term of $q_z(z)$ along the x-axis (equation (10)). The $q_z(z)$ term is also a gaussian distribution term with the total heat flux input $\boldsymbol{\beta\eta VI}$ as the coefficient term and the distributor term along the z-axis. $q_z(z)$ distributes the total heat flux input along the z axis points and the term $q_d(x)$ further distributes the heat flux input along the x-axis.

$$q_s(x,z) = q_z(z).(\frac{1}{\sqrt{2\pi}R}\exp{\left[-\frac{1}{2}(\frac{x}{R})^2\right]}) \qquad (9)$$

$$\text{where } q_z(z) = (\frac{\beta\eta VI}{\sqrt{2\pi}R}\exp{[-\frac{1}{2}(\frac{z-z_i}{R})^2]} \qquad (10)$$

$$\text{and } q_d(x) = \frac{1}{\sqrt{2\pi}R}exp{\left[-\frac{1}{2}(\frac{x}{R})^2\right]} \qquad (11)$$

For the modified heat source model that incorporates the arc elongation effect for bead-on-bead deposition, the $q_z(z)$ term remains unchanged as the length of the bead along z-axis is generally long enough to consider it as a flat surface and a gaussian distribution holds good. The $q_d(x)$ is modified to include both x and y terms as the heat input varies along the y-axis as well. *An empirical correlation to get the $q_d(x)$ can be developed using surface temperature data $T(x')$ from spectroscopy experiment of the WAAM process.* Here x' represents a transformed coordinate system where the perimeter of the deposited beads is taken as the x' axis (Figure 3.11). Using the new coordinate transformation we get-

$$q_s'(x, z) = q_z(z) \cdot q_x(x')$$ (12)

To obtain the empirical expression for $q_x(x')$ using $T(x')$, the $T(x')$ relation will be scaled by a factor of k such that the area under the graph equals the total heat flux input for all points in x-axis at that z coordinate.

$$q_x(x') = K \cdot T(x')$$ (13)

Under the condition that $\int_{-\infty}^{\infty} K \cdot T(x') dx' = q_z(0)$ (14)

$$K \cdot \int_{-\infty}^{\infty} T(x') \, dx' = q_z(0)$$

$$K = \frac{q_z(0)}{\int_{-\infty}^{\infty} T(x') dx'}$$ (15)
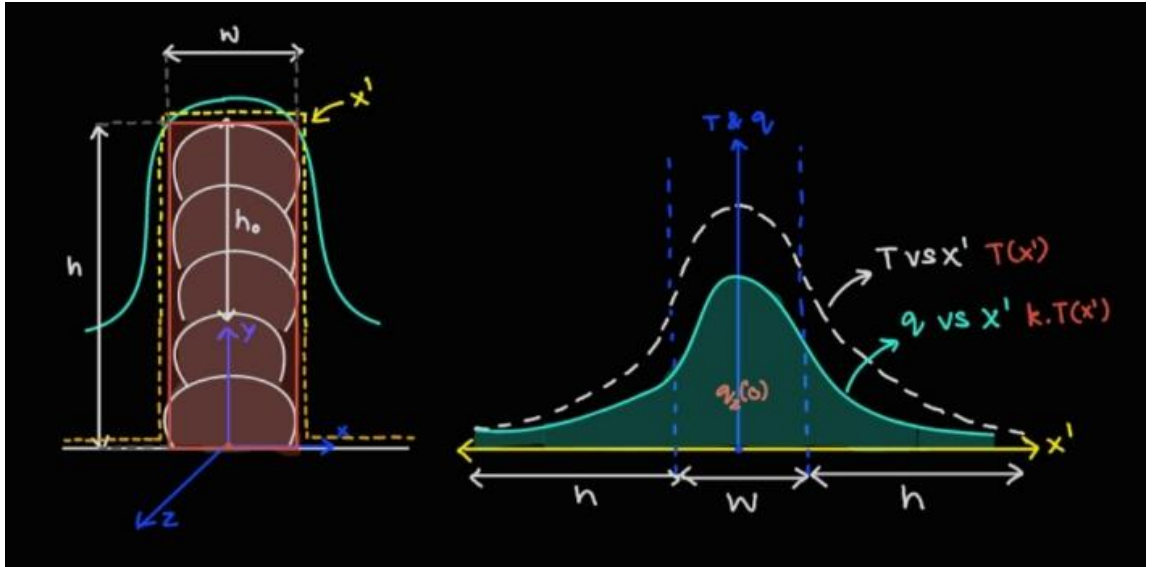
[Figure3.11: 3.11.A.(left) illustrates the rectangular approximation approach used to model the temperature and heat flux input along the outer perimeter of the beads. The temperature data along the *x'* (shown in dotted yellow line) is captured; Figure 3.11.B. (right) shows the temperature data (shown in dotted white curve) and the empirical correlation obtained for *qx(x')* (shown in green curve) plotted in the transformed *x'* axis.]

For convenience we assume there are no creases and taking bead profiles to be rectangle and considering $q_s(z, x)$ to be a step function containing 3 domains- $q_{s1}(z, x)$ for the topmost bead, $q_{s2}(z, y)$ for the side walls and $q_{s3}(z, x)$ for the base plate. Depending on the $h - h_0$ values the $q_{s3}(z, x)$ term can be neglected as at higher values of h, the arc doesn't reach the base plate or even few of the initial layers.

$$q_{s1}(z, x) = q_z(z) \cdot q_x'(x) \quad \text{For, } x' \epsilon \ (\tfrac{-w}{2}, \tfrac{w}{2}) \tag{16}$$

$$q_{s2}(z, y) = q_z(z) \cdot q_x'(y - h + 2h_0 + \frac{w}{2}) \quad \text{For, } x' \epsilon \ (\tfrac{w}{2}, \tfrac{w}{2} + h) \tag{17}$$

$$q_{s3}(z, x) = q_x'(x + h_0 + \frac{w}{2}) \quad \text{For, } x \epsilon \ (-\infty, \tfrac{-w}{2}) \cup (\tfrac{w}{2} + \infty) \tag{18}$$

The following equations (16-18) is used as the *surface heat flux condition* for the FEA simulation for the corresponding surfaces to achieve a higher correlation with the experimental temperature curves recorded and to accurately predict thermal cycles and thus the microstructure properties.

CHAPTER 4

ANALYTICAL MODELLING

4.1 Introduction

This chapter explains the analytical approach adopted to model thermal cycles in a WAAM component. While numerical modeling provides results with agreeable accuracy, the method is very computationally intensive and time-consuming. The analytical solution developed, can predict thermal cycles, weld-pool, and HAZ dimensions with reasonable accuracy. This work utilized models developed on Rosenthal's 3D moving heat source equation, recalculated with Goldak's double ellipsoidal volumetric heat source model and the model was implemented in python. The study starts with modeling single-pass welding and then proceeds to multi-pass welds which form the basis for additive manufacturing. The thermal cycle data thus obtained will further be used to predict the metallurgical properties of the WAAM process.

Figure 4.1: Routemap of the analytical modeling process.
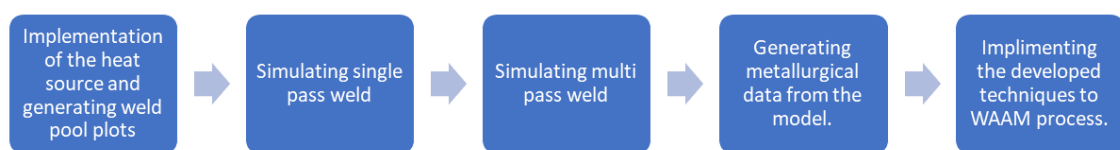
4.2 The heat source model

For the analytical model, a double ellipsoidal volumetric heat source is considered here with semi-infinite body approximations, as considered by [Nguyen, et al (2004)]. The double ellipsoidal heat source [equation (4.2-4.4)] used in our study is a derivative of the semi ellipsoidal heat source with Gaussian heat flux distribution [Goldak et.al

(1984)] shown in equation (4.1).
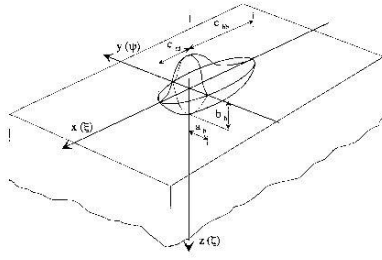
$$Q(x, y, z) = \frac{6\sqrt{3}\eta VI}{a_h\, b_h c_h \pi \sqrt{\pi}} \exp\left(-\frac{3x^2}{c_h{}^2} - \frac{3y^2}{a_h{}^2} - \frac{3z^2}{b_h{}^2}\right)$$

(4.1)

Figure 4.2: Goldak Heat Source

Where a_h, b_h, c_h are the dimensions of the considered heat source width/ minor axis, depth, and major axis respectively (in the case of semi ellipsoid), as shown in Figure 4.2 and V, I, η are the welding voltage, current, and efficiency respectively.

The semi ellipsoidal model however gave incorrect predictions of the steepness of the temperature variations [Goldak et.al (1984)], therefore a double ellipsoidal heat source was developed, combining two different semi ellipsoids, for the front and rear parts of the arc as shown in equations (4.2-4.4)

$$Q_f(x, y, z) = \frac{6\sqrt{3}r_f Q}{a_h\, b_h c_{hf} \pi \sqrt{\pi}} \exp\left(-\frac{3x^2}{c_{hf}{}^2} - \frac{3y^2}{a_h{}^2} - \frac{3z^2}{b_h{}^2}\right)$$

(4.2)

$$Q_b(x, y, z) = \frac{6\sqrt{3}r_b Q}{a_h\, b_h c_{hb} \pi \sqrt{\pi}} \exp\left(-\frac{3x^2}{c_{hb}{}^2} - \frac{3y^2}{a_h{}^2} - \frac{3z^2}{b_h{}^2}\right)$$

(4.3)

$$Q(x, y, z) = \frac{6\sqrt{3}Q}{a_h\, b_h \pi \sqrt{\pi}} \left(\frac{r_f}{c_{hf}} \exp\left(-\frac{3x^2}{c_{hf}{}^2} - \frac{3y^2}{a_h{}^2} - \frac{3z^2}{b_h{}^2}\right) + \right.$$

(4.4)

$$\left. \frac{r_b}{c_{hb}} \exp\left(-\frac{3x^2}{c_{hb}{}^2} - \frac{3y^2}{a_h{}^2} - \frac{3z^2}{b_h{}^2}\right)\right)$$

Where a_h, b_h, c_{hf}, c_{hb} are the double ellipsoidal heat source parameters as described in Figure 4.2, $Q = \eta IV$ is the arc heat input, r_f, r_f the proportional coefficients for the front and back ellipsoids respectively. It is important to notice that here the heat source model is defined by the following five parameters $a_h, b_h, c_{hf}, c_{hb}, \eta$. Also, $\frac{r_f}{c_{hf}} = \frac{r_b}{c_{hb}}$, furthermore, $r_f + r_b = 2$.

4.3   Nguyen's model for temperature field.

The solution for temperature gradient for this heat source can be obtained by integrating the solution for an instantaneous heat source, satisfying the heat conduction equation in fixed coordinates. Now the temperature rises due to a very short time increment dt' from time t' caused by an infinitesimally small heat addition Qdt' can be estimated by integrating the following equation (4.6)

$$dT_{t'} = \frac{3\sqrt{3}Qdt'}{\rho c \pi \sqrt{\pi}} \cdot \frac{1}{\sqrt{12a(t-t')+a_h^2}} \cdot \frac{1}{\sqrt{12a(t-t')+b_h^2}} \cdot \frac{1}{\sqrt{12a(t-t')+c_h^2}} \exp\left(-\frac{3x^2}{12a(t-t')+c_{hf}^2} - \right.$$

$$\left. \frac{3y^2}{12a(t-t')+a_h^2} - \frac{3z^2}{12a(t-t')+b_h^2}\right)$$

(4.6)

Here $a = \frac{k}{\rho c}$, k=thermal conductivity and ρ = mass density t , t' are time variables with t' varying from 0 to t , and $dT_{t'}$ is the small temperature change. The total temperature change here can be found for each point (x, y, z) from the temperature gradient equation, obtained by integrating the changes over the double ellipsoid considering it is moving with a speed v for a duration $t' = 0$ to $t' = t$, and the result can be obtained as follows [Nguyen, et al (2004)].

$$T - T_0 = \frac{3\sqrt{3}Q}{2\rho c \pi \sqrt{\pi}} \int_0^t \frac{dt'}{\sqrt{(12\mathrm{K}(t-t')+a^2)(12\mathrm{K}(t-t')+b^2)}} \left(\frac{A'}{\sqrt{12\mathrm{K}(t-t')+c_f^2}} + \frac{B'}{\sqrt{12\mathrm{K}(t-t')+c_r^2}}\right)$$

(4.7a)

Where,

$$A' = r_f \exp\left(-\frac{3(z-vt')^2}{12\mathrm{K}(t-t')+c_{hf}^2} - \frac{3x^2}{12\mathrm{K}(t-t')+a_h^2} - \frac{3y^2}{12\mathrm{K}(t-t')+b_h^2}\right)$$

(4.7b)

$$B' = r_b \exp(-\frac{3(z-vt')^2}{12\mathrm{K}(t-t')+c_{hb}^2} - \frac{3x^2}{12\mathrm{K}(t-t')+a_h^2} - \frac{3y^2}{12\mathrm{K}(t-t')+b_h^2}) \qquad (4.7c)$$

In our analytical simulation, we are numerically integrating the temperature field and hence the weld pool and weld isotherms are estimated. By varying the coordinates, we can estimate the temperatures and cooling characteristics of a single pass weld, as well as the effect of various parameters on the weld pool dimensions.

4.4 Facinotti's model for temperature field.

Nguyen's model approximated the effects of asymmetry of the heat source by averaging the results of spacial integrals with both c_{hf} and c_{hb} respectively in the limits $-\infty$ to $+\infty$. Though this approximation gave an estimate not too far from expected values, this introduced errors, as this holds only in cases when $c_{hf} = c_{hb}$. Facinotti et. al. addressed this issue by integrating equation (4.9), from $-\infty$ to 0, and (4.10) from 0 to $+\infty$

$$dT_{t'} = \frac{3\sqrt{3}Qdt'}{\rho c\pi\sqrt{\pi}} \cdot \frac{1}{\sqrt{12a(t-t')+a_h^2}} \cdot \frac{1}{\sqrt{12a(t-t')+b_h^2}} \cdot \frac{1}{\sqrt{12a(t-t')+c_h^2}} \exp\left(-\frac{3x^2}{12a(t-t')+c_{hf}^2} - \right.$$
$$\qquad (4.9)$$
$$\left. \frac{3y^2}{12a(t-t')+a_h^2} - \frac{3z^2}{12a(t-t')+b_h^2}\right)$$

$$dT_{t'} = \frac{3\sqrt{3}Qdt'}{\rho c\pi\sqrt{\pi}} \cdot \frac{1}{\sqrt{12a(t-t')+a_h^2}} \cdot \frac{1}{\sqrt{12a(t-t')+b_h^2}} \cdot \frac{1}{\sqrt{12a(t-t')+c_h^2}} \exp\left(-\frac{3x^2}{12a(t-t')+c_{hb}^2} - \right. \qquad (4.10)$$
$$\left. \frac{3y^2}{12a(t-t')+a_h^2} - \frac{3z^2}{12a(t-t')+b_h^2}\right)$$

The resulting temperature field equation is obtained as in equation (4.11),

$$T(x,y,z,t) = T_0 + \frac{6\sqrt{3}}{\pi\sqrt{\pi}}\frac{Q}{\rho c}\int_0^t \frac{\exp\left(-3\frac{x^2}{12\kappa(t-t')+a^2}-3\frac{y^2}{12\kappa(t-t')+b^2}\right)}{\sqrt{12\kappa(t-t')+a^2}\sqrt{12\kappa(t-t')+b^2}}[r_b A_b(1-B_{r)} +$$
$$\qquad (4.11a)$$

$$r_f A_f (1 + B_f)] dt'$$

Where,

$$A_i = A(z, t, t'; c_i) = \left(\frac{\exp\left(-3\frac{(z-vt)^2}{12\kappa(t-t')+c_i^2}\right)}{\sqrt{12\kappa(t-t')+c_i^2}} \right) \tag{4.11b}$$

$$B_i = \text{erf}[\frac{c_i}{2} \frac{(z-vt')}{\sqrt{\kappa(t-t')}\sqrt{12\kappa(t-t')+c_i^2}} \tag{4.11c}$$

This solution can fully emulate the theoretical concept of the double ellipsoidal heat source and was utilized in the model.

4.5 Displacement scaled model

When the above models were implemented and extensive comparison with experimental data was performed, we could observe a significant deviation in cooling rates, and thus the time-temperature profiles for the welds. To correct this a mathematical investigation was done. We can express the temperature difference from starting temperature in the current model as in equation 4.12 described below.

$$\Delta \text{T}(x, y, z, t) = \frac{3\sqrt{3}}{4\pi^3} \frac{Q}{\rho c K^{3/2} ab} \int_0^t I_x I_y (\frac{f_r}{c_r} I_z^r + \frac{f_f}{c_f} I_z^f)(t-t')^{-\frac{3}{2}} dt' \tag{4.12}$$

Here, I_x, I_y, I_z^f, I_z^r are of the form $I_x = exp[-3\frac{x'^2}{a^2} - \frac{(x-x')^2}{4K(t-t')}] dx$. On converting this to the standard form of $\int_{-\infty}^{\infty} \exp(-ax^2 + bx + c)$, $a \geq 0$ and integrating the expression in polar coordinates, we can obtain solutions as obtained below.

$$I_x, I_y, I_z^f, I_z^r = \sqrt{\frac{\pi}{A}} \exp\left(\frac{B^2}{4A} + C\right) \tag{4.13}$$

Here,

$$A = \frac{12\text{K}(t - t') + a^2}{4\text{K}a^2(t - t')} \tag{4.13a}$$

$$B = \frac{x}{2\text{K}(t - t')} \tag{4.13b}$$

$$C = \frac{x^2}{4\text{K}(t - t')} \tag{4.13c}$$

This will yield x, y, z distribution terms of the form,

$$\exp\left(-\frac{x^2}{12\text{K}(t - t') + a^2}\left(3 + \frac{a^2}{4\text{K}}\left(1 + \frac{1}{(t - t')}\right)\right)\right) \tag{4.14}$$

The referred papers make a simplification here and neglect the extra terms to obtain the final equations as in equations 4.7,4.11. This approximation is valid while calculating temperatures at points near to weld center. But in our use case points much further need to be included, this makes some sort of correction to this approximation necessary based on the observations. Here is an empirical relation between the proposed models and new equations are derived based on a correction factor f, and the modified equation in the final model used are as follows.

$$T(x, y, z, t) = T_0 + \frac{6\sqrt{f3}}{\pi\sqrt{\pi}} \frac{Q}{\rho c} \int_0^t \frac{\exp\left(-3\frac{fx^2}{12\kappa(t-t')+a^2} - 3\frac{fy^2}{12\kappa(t-t')+b^2}\right)}{\sqrt{12\kappa(t-t')+a^2}\sqrt{12\kappa(t-t')+b^2}} [f_r A_r(1 - B_{r)} + \tag{4.15a}$$

$$f_f A_f\left(1 + B_{f)}\right]dt'$$

$$A_i = A(z, t, t'; c_i) = \left(\frac{\exp\left(-3\frac{f(z-vt)^2}{12\kappa(t-t')+c_i^2}\right)}{\sqrt{12\kappa(t-t')+c_i^2}}\right) \tag{4.15b}$$

$$B_i = \text{erf}\left[\frac{c_i}{2}\frac{(z - vt')\sqrt{f}}{\sqrt{\kappa(t - t')}\sqrt{12\kappa(t - t') + c_i^2}}\right] \tag{4.15c}$$

These same corrections were applicable with Nguyen's approximation as well and some simulations were performed with the modified equations derived from this model as per the equation below.

$$T - T_0 = \frac{6\sqrt{f3}Q}{2\rho c\pi\sqrt{\pi}} \int_0^t \frac{dt'}{\sqrt{(12K(t-t')+a^2)(12K(t-t')+b^2)}} \left(\frac{A'}{\sqrt{12K(t-t')+c_f^2}} + \frac{B'}{\sqrt{12K(t-t')+c_r^2}} \right)$$ (4.16a)

Where,

$$A' = f_f\exp(-\frac{3f(z-vt')^2}{12K(t-t')+c_f^2} - \frac{3fx^2}{12K(t-t')+a^2} - \frac{3fy^2}{12K(t-t')+b^2})$$ (4.16b)

(4.16c)

$$B' = f_r\exp(-\frac{3f(z-vt')^2}{12K(t-t')+c_r^2} - \frac{3fx^2}{12K(t-t')+a^2} - \frac{3fy^2}{12K(t-t')+b^2})$$

There are still scopes for improvement in this, and implementing the complete equation is also in the scope of this study which can be amended in upcoming research on this topic.

4.6 Multi-pass welding simulation

A multi-pass weld is simulated by considering it as a series of single-pass welds with overlapping beads. The simulation first weld-pass starts at the pre-heating temperature and the subsequent weld-passes at inter-pass temperature, not that inter-pass temperature will always be greater than or equal to the preheating temperature. Now the interesting characteristics here are emerging from the heat treatment effect caused by the later weld-passes on the previously deposited weld-passes. In some beads remelting occurs whereas in others the temperature goes to the austenitization temperature where solid to solid phase transformations occurs. To tackle this issue in the model, we need to recalculate all the regions which come under the weld pool of the latest weld pool along with its heat-affected zone (HAZ). Set theory is utilized here to tackle this issue. The model starts with a defined number of discrete elements to

36

calculate temperatures ON and consequently according to the temperatures obtained from equation (4.7), different sets of points are created. Whenever a new weld-pass is performed, the set of points in its remelting and significant HAZ zones are calculated. The set of points in the significant HAZ zone can be calculated by evaluating the relation $T \leq T_\gamma + T_i < T_m$, where T_γ is the transformation temperature limit (like 500℃ for steel where 800 to 500 is the transformation temperature range known as t_{8-5}), T_i is the inter-pass temperature, T_m is the melting point of the weld material and T is the estimated temperature value. Now the regions are separated by finding the intersection between the required regions. As per equation (4.8), the body points are separated.

$$P_{body} = P_{body} \sim P_{body} \cap (P_{HAZ} \cup P_{remelting})$$
(4.8)

4.7 Optimized Multi-pass welding simulation

To get the thermal cycles of the weld, which is of prime importance, equation (4.7) provides an interesting temperature gradient function which is a summation of two different heat distributions from two ellipsoidal sections. Now although this makes this equation continuous it is not differentiable and hence finding the peak temperature by applying calculus is not possible. Similarly, solving for the exponential terms for the probability distribution functions A', B' from equations 4.7(a), (b), directly is also complicated. However, by the nature of exponential functions, the maximum temperature can be obtained when the distributer terms attain their maximums, and this happens when the term inside the exponential expression is zero,

$$\frac{\exp\left(-\frac{3(x-vt')^2}{12a(t-t')+c_{hf}^2}-\frac{3y^2}{12a(t-t')+a_h^2}-\frac{3z^2}{12a(t-t')+b_h^2}\right)}{f_A(t')}+\frac{\exp\left(-\frac{3(x-vt')^2}{12a(t-t')+c_{hb}^2}-\frac{3y^2}{12a(t-t')+a_h^2}-\frac{3z^2}{12a(t-t')+b_h^2}\right)}{f_B(t')}$$
(4.9a)

$$f_A(t') = \frac{r_f}{\sqrt{12a(t-t')+c_{hf}^2}}$$
(4.9b)

$$f_B(t') = \frac{r_b}{\sqrt{12a(t-t')+c_{hb}^2}}$$
(4.9c)

Here $f_A(t')$, $f_B(t')$ are the denominator functions in equation (4.7), Also from the model of the heat source, $f_A(t') < f_B(t')$. This implies if the symmetrical heat source equation was to be considered, where only one exponential term exists the maximum temperature occurs directly when the arc center reaches that particular point. But for a double ellipsoidal heat source as the heat input is not symmetrical, there is a certain time difference between when the origin of the moving heat source reaches a particular point and when it reaches the maximum temperature. But this temperature difference can be assumed to be constant for all points that are located sufficiently away from the boundaries due to the identical conditions experienced by all these points locally. Therefore, a first-order approximation is done to arrive at an empirical relation for the value of t at the peak temperature.

$$f_A(t') = \frac{r_f}{6at + c_{hf}^2 + 0.5 - 6at'} \qquad (4.10a)$$

$$f_B(t') = \frac{r_b}{6at + c_{hb}^2 + 0.5 - 6at'} \qquad (4.10b)$$

Now, as t' increases the other overall expression deteriorates exponentially, and only at smaller values of t' does the term contain relevance, hence the term can be approximated to a constant k'' now if we say $k'' = e^{k'}$, and considering weld direction as x, we know the center of the weld will always have a maximum temperature so, at $y = 0$, $z = 0$ conditions, our distributor functions are,

$$\exp\left(-\frac{3(x - vt')^2}{12a(t - t') + c_{hf}^2} - k'\right) + \exp\left(-\frac{3(x - vt')^2}{12a(t - t') + c_{hb}^2} - k'\right) \qquad (4.11)$$

Now the maximum of this function occurs when $x + k - vt' = 0$, hence,

$$t_p = \frac{x}{v} + \frac{k}{v} \qquad (4.12)$$

Here k is an empirical constant that is estimated with the help of the simulation. With

the help of t_p the cooling curves and heating curves are distinguished, and the thermal cycles are plotted with appropriate logical conditions. The calculated peak temperature is used to decide whether a particular point is its heating cycle or cooling cycle. More importantly, it greatly reduces the simulation time by acting as a functional computational filter to remove redundant points which have already reached their peak temperature from the analysis.
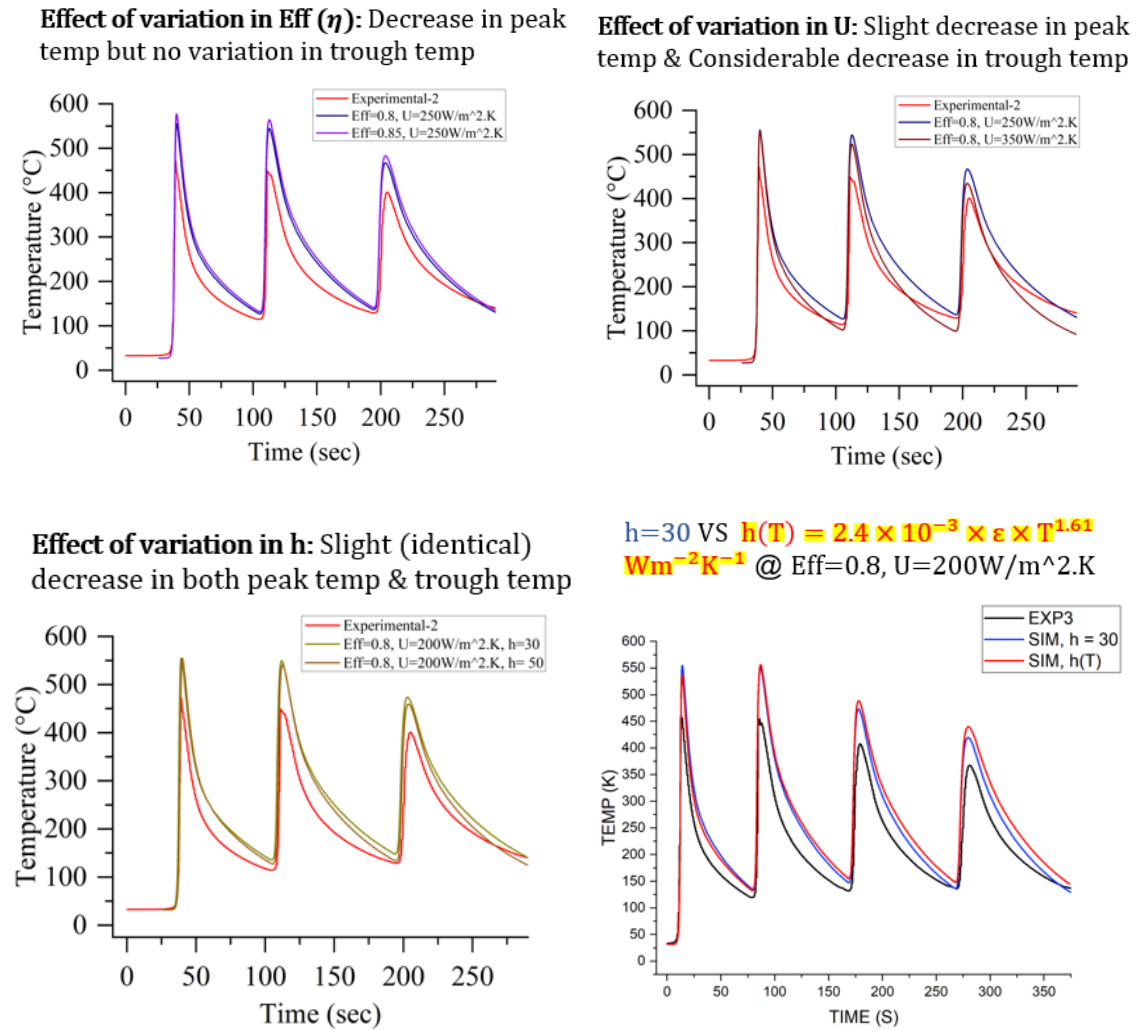

[Figure 4.3: Robotic SAW welder setup and DAQ system used for experiments]

CHAPTER 5

RESULTS AND DISCUSSION

5.1 Numerical Modelling

To evaluate the accuracy of the developed numerical model the predicted thermal cycle data is compared with the thermal cycle data obtained from the experiments done by Chaitanya et al. (BTP 2021). The 3 important factors to check the correlation are: The peak points, the valley points and the cooling rates.

Effect of variation in Eff (η): Decrease in peak temp but no variation in trough temp

Effect of variation in U: Slight decrease in peak temp & Considerable decrease in trough temp

Effect of variation in h: Slight (identical) decrease in both peak temp & trough temp

h=30 VS $h(T) = 2.4 \times 10^{-3} \times \varepsilon \times T^{1.61}$ $Wm^{-2}K^{-1}$ @ Eff=0.8, U=200W/m^2.K

[Figure 5.1.1: The plots show the variation of Temperature Data with change in

simulation parameters like Effeciency, Base plate Heat Transfer Coeficient, Overall Convective Heat Transfer Coeficient and Temperature Dependent Convetive Heat Transfer Coeficient.]

Multiple simulations were done by variying the parameters like Effeciency, Base plate Heat Transfer Coeficient, Overall Convective Heat Transfer Coeficient and Temperature Dependent Convetive Heat Transfer Coeficient to observe how they affect the resulting Thermal cycles. The results are shown in Figure 5.1. We can observe that best corelation is observed while using the parameters: *Eff = 0.8, U = 200* $Wm^{-2}K^{-1}$ *and* $h = 2.4 \times 10^{-3} \times \varepsilon \times T^{1.61} \, Wm^{-2}K^{-1}$.

5.2   Analytical Modeling

With the help of equation (7) an analytical model is developed from scratch to predict the weld pool geometry to observe the effects of various factors that affect it. Figure (5.1) shows the weld pool dimensions that are generated by the developed model. Figure (5.2.A) Shows the weld penetration results obtained from the developed model. In the next step, the variation of weld pool dimensions is studied, in accordance with the variation in the ah parameter, as visualized in Figure (5.2.B).
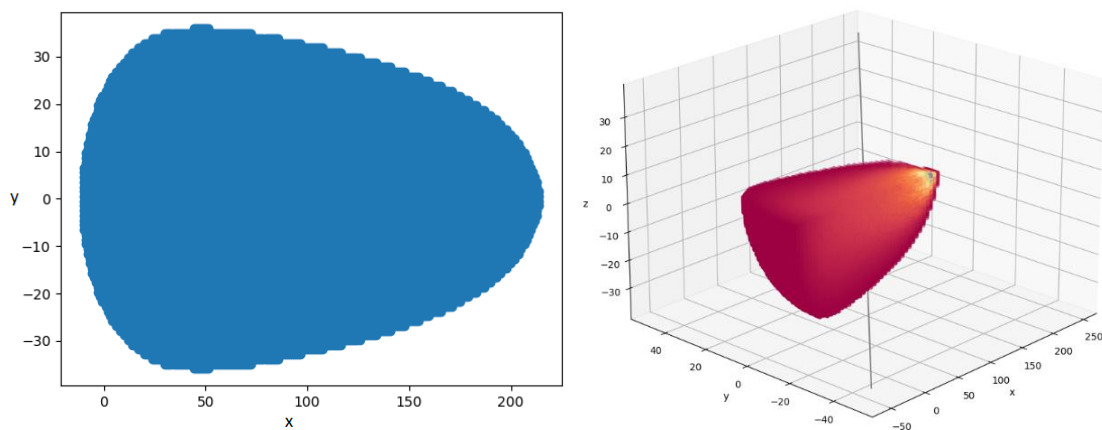
[Figure 5.1: weld pool dimensions obtained from our computational model in XY directions (left). the welding is done along the x-direction, colormap represents the temperature gradient (right).]
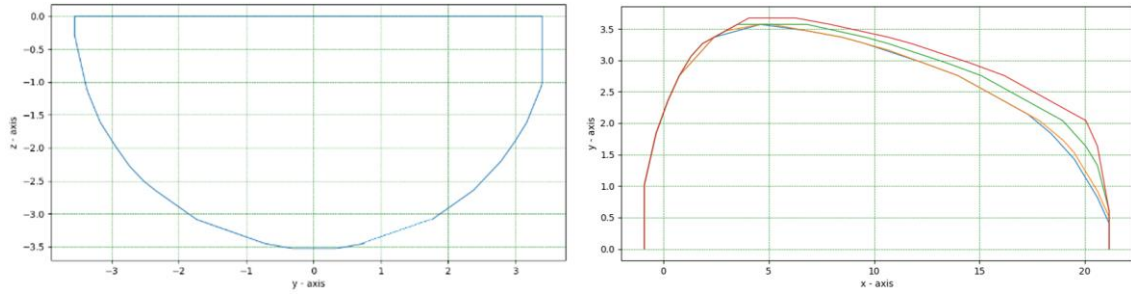
[Figure 5.2.A: Representation of y-z dimensions of the weld pool depicting weld penetration. All units are in mm; Figure.5.2.B: Weld pool boundary with varying values of *ah* parameters ah=3,6,15,21 is shown as blue, orange, green, red respectively, scale =1, all units in mm.]

It is clearly observable that as the value of a_h increases the weld pool is enclosing more area. This is due to the more decentralized distribution of the instantaneous heat sources in the model, which essentially heats up more parts of the base metal. The graphical representations here are based on a fixed time snap of the heat distribution at $t = 30s$. For more accurate and faster computation all the isotherms have to be calculated at $t = t_p$.
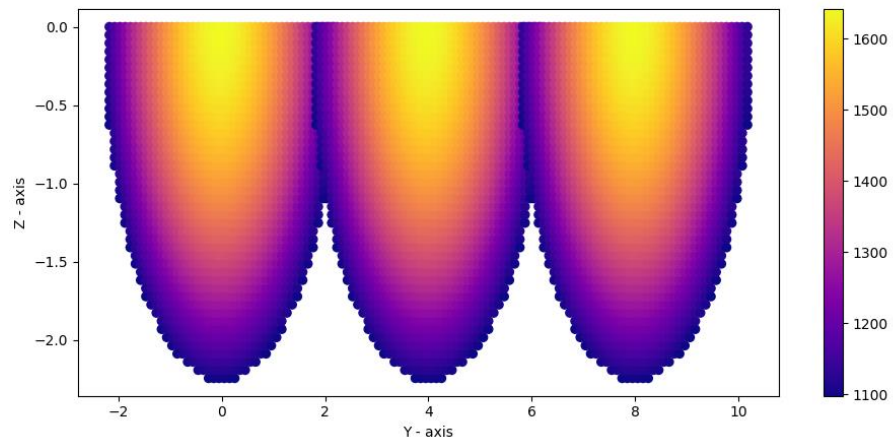
[Figure5.3: Multi-pass weld initial stage simulation.]

Figure 5.3 shows the temperature gradient for multi-pass weld, this was partly successful however the data produced in the overlapping region was not accurate since the thermal cycles were yet to be incorporated as discussed below.

5.2.1 Thermal cycle simulation

Figure 5.4 shows the comparison of results from the developed model to the experimental findings from the works of N.T.Nguyen et al.(2004). Since the work addressed a similar Goldak heat source, obtaining the necessary parameters was feasible. The analysis was done on the points $A(x, y, z) = (67,0,1)$ and $B(x, y, z) = (60,0,2)$. Table-1 shows the parameters for the simulation and figure (5.4) shows the results side by side with the results from Nguyen's simulations and experimental data.

Table 5.1: Simulation parameters:

Parameter	value
z offset	1 mm
a_h	10mm
b_h	2mm
c_{hf}	10mm
c_{hb}	20mm
η	85%
c	600$J/kg°C$
k	29 $J/ms°C$
ρ	7820 kg/m^3
a	6.181E-6
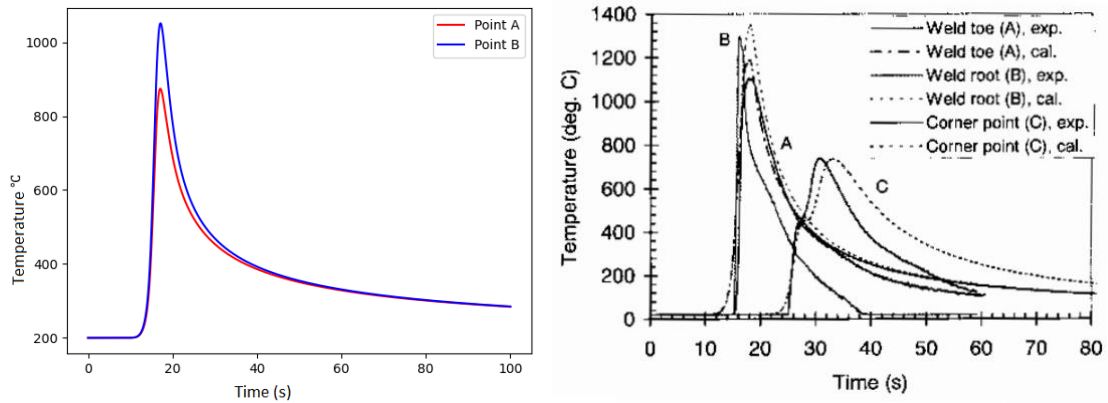
[Figure 5.4: Results generated from our model (left), results generated from Nguyen's model (right).]

5.2.2 t_p Estimation

To model multipass weld knowing the peak temperature and the time of its occurrence is important to distinguish between the heating and cooling cycles. So the model is using the empirical relation obtained from the linear approximation. Figure (5.5) shows that the approximation is well within acceptable limits with a deviation of 6.3% on average, which is being addressed by refining the process.
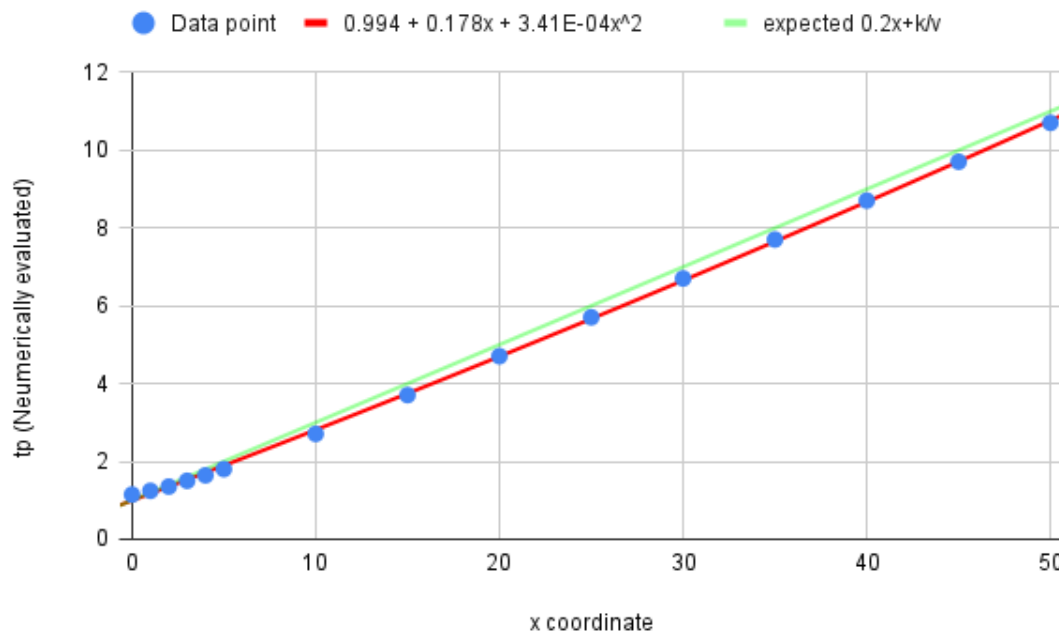
[Figure 5.5: Comparison of numerical data obtained for t_p with the predicted empirical curve the blue dots represents data from numerical evaluation, x in mm]

44
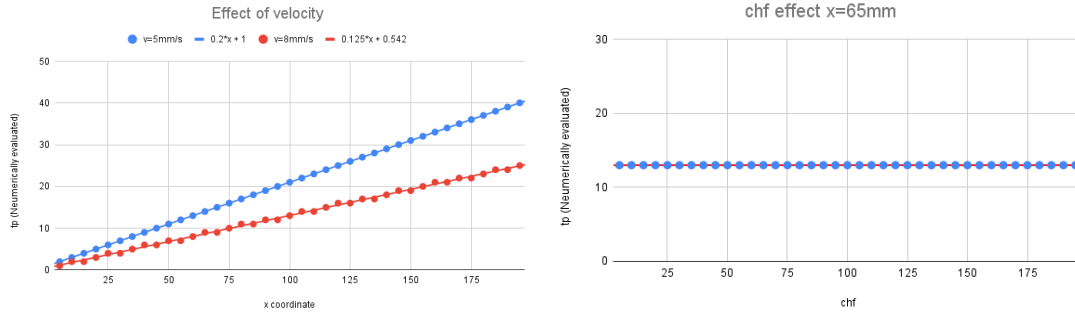
[Fig 5.6: Effect of velocity (left) and (c_{hf}) on tp.]

5.2.3 Multi pass-welding thermal simulation

Now that calculating the peak temperature is possible, multi-pass thermal cycles are simulated and the resulting curves resemble experimentally obtained curves mentioned in the literature. Further data collection is needed to perform correlation analysis on these results

45
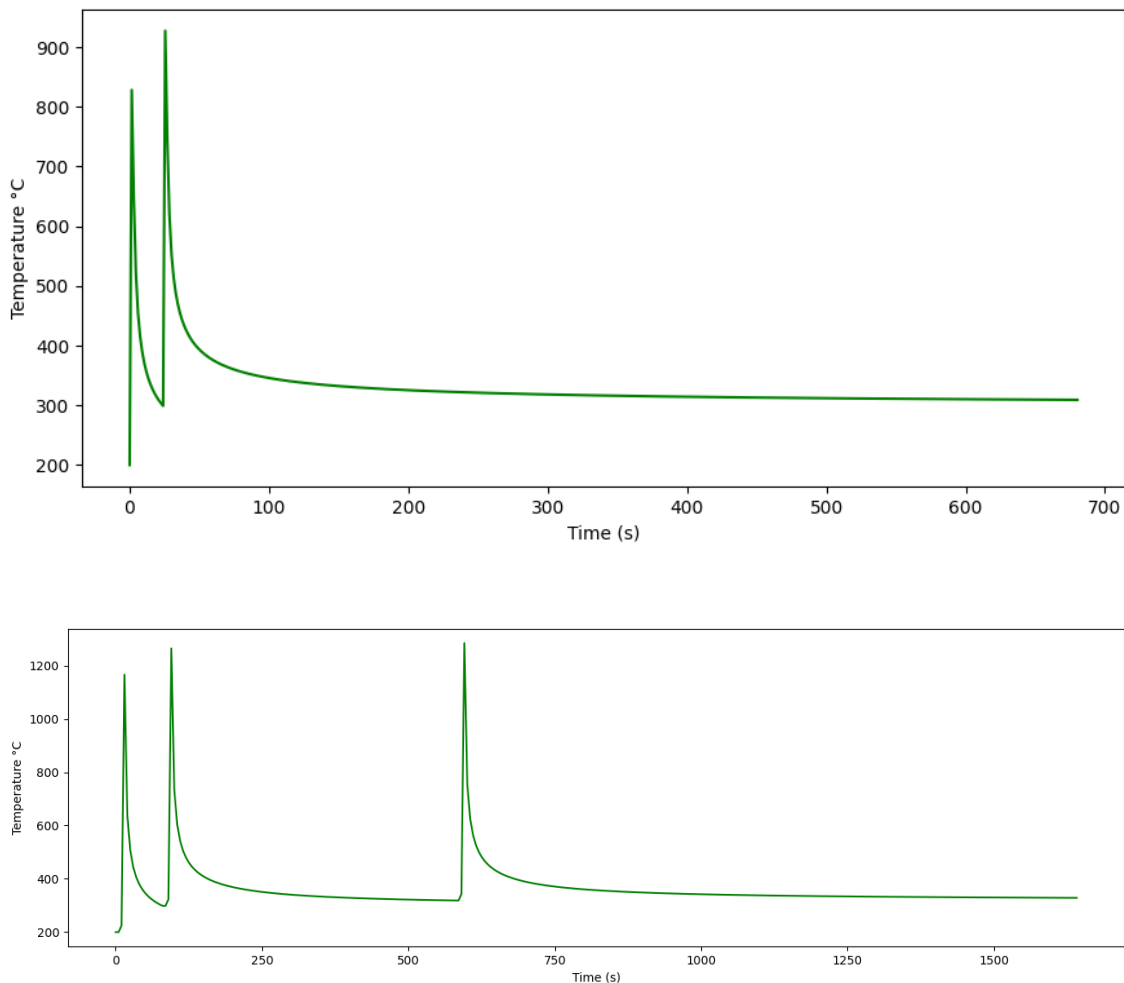
[Figure 5.7: Multi-pass thermal cycles for 2 passes (Top), 3 passes (Bottom)]

The peak temperature expression is used to check if the point is currently in the heating phase of the cooling phase of the thermal cycle. Later on, this would also help as a filter to decide which points are to be considered for metallurgical transformations as explained in section 1.8. As the next step of the simulation, the models generating thermal cycles and weld pools are to be combined, and the final model should be able to generate spatial and temporal data accurately before moving on to the metallurgical transformations.

5.2.4 Faccinotti vs Nguyen

Results obtained from the implementation of Nguyen's and Faccinotti's are reviewed to see how much of an advantage the added computational time and complexity of the latter gives in terms of the accuracy of predictions it makes.
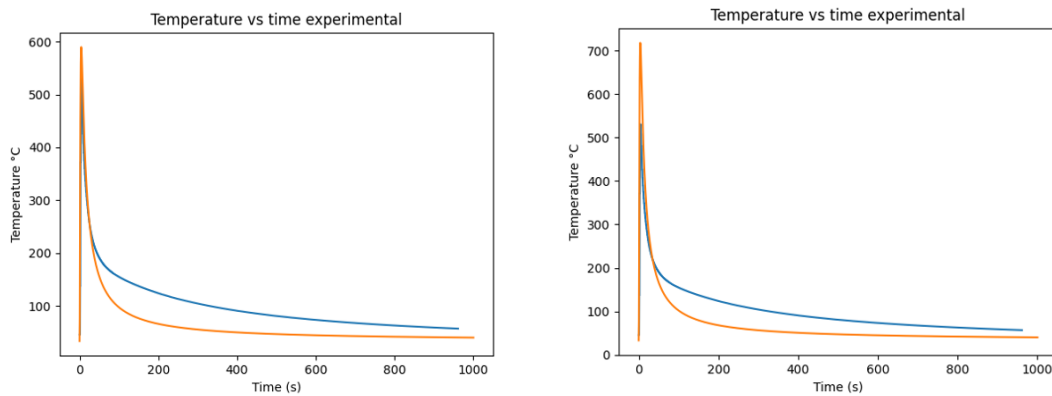
[Figure 5.8: Single-pass thermal cycles for Nguyen (Right), Facinotti (Left). Blue and orange lines represent experimental and simulated curves respectively.]

From figure 5.8, we can observe that Facinotti's model gives better results at higher temperatures, though Nguyen's model generated results following the experimental curve closely, the error it makes in peak temperature prediction is significant. Quantitatively, it is almost 25% more accurate, by reducing the error from 36% to 11%.

This actually validated the extra computational effort that has been put into calculating the model over Nguyen's.

5.2.5 Displacement scaled model

The displacement scaling correction was implemented after a thorough study of the deviations observed from simulating a set of 28 thermocouples in 16 different configurations. The deviation in cooling rates for larger displacements was clearly observable, as shown in figure 5.9 below.
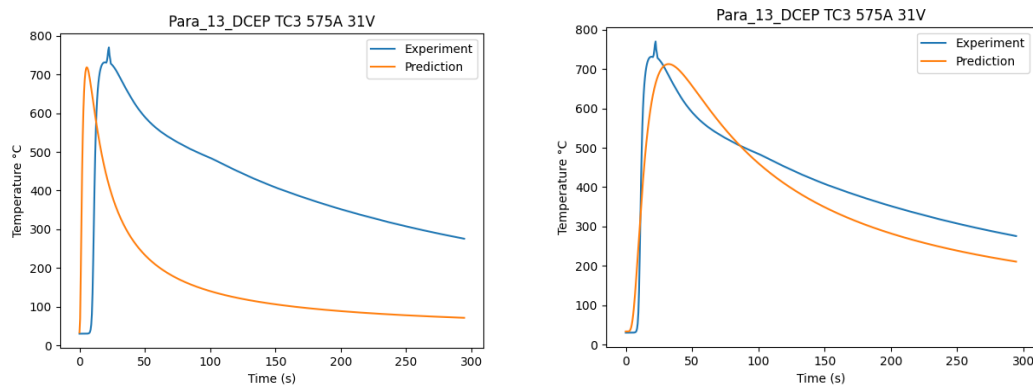

[Figure 5.9: Experimental vs prediction Facinotti (Left), Displacement scaled (Right).]

From the cycles, T8-5 cooling times, as well as peak temperatures, were also obtained, and the data was compiled. Figure 4.3 shows the experimental setup.
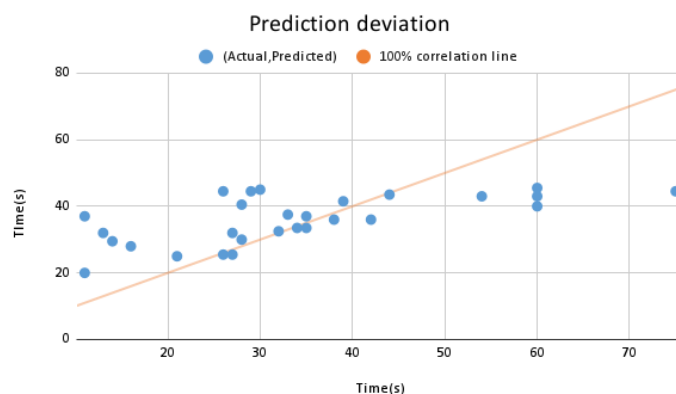
[Figure 5.10: T8-5 cooling times for all experiments]

The distribution of predictions of the updated model can be understood from the above plot. A comparison of the model with the previously discussed one as they were implemented is also visualized as histograms below.
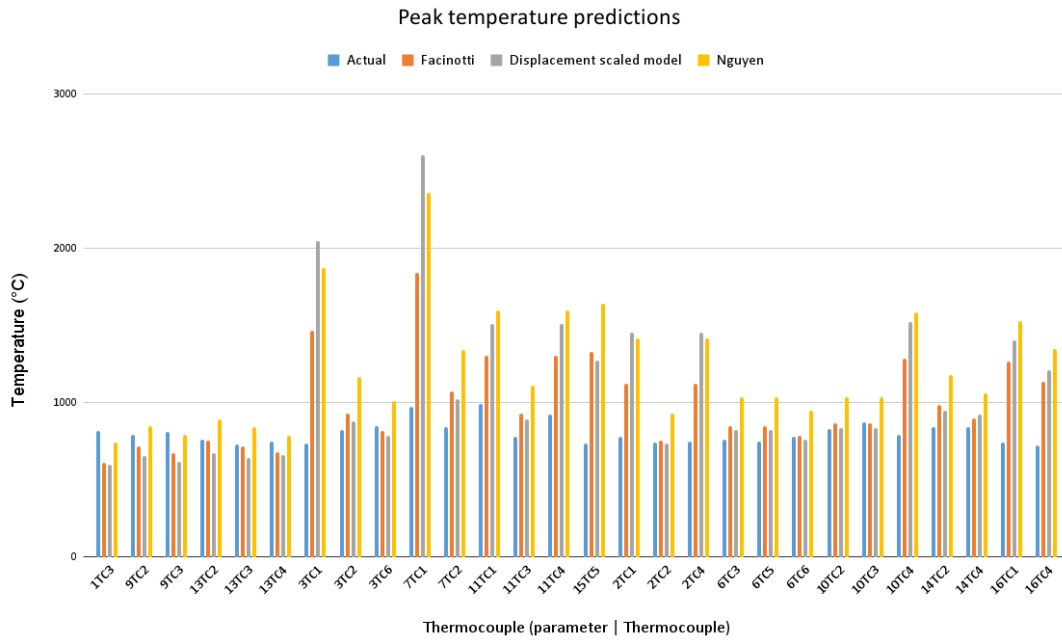

[Figure 5.11: Peak temperature predictions for all experiments]

There are some outlier cases due to errors in experiments and other circumstantial factors, however, the model is able to give conforming results for the most part.
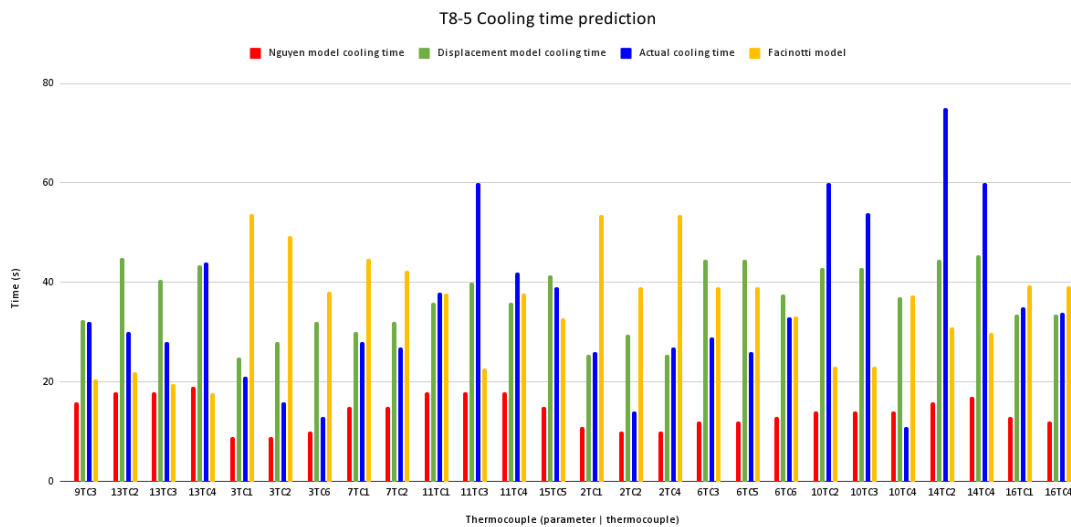

[Figure 5.12: T8-5 predictions for all experiments]

The abovementioned experiments are done by drilling and implanting thermocouples in the viscera of the base metal. A set of simulations were performed for surface-mounted thermocouples as well, and the model could predict the results with reasonable conformity here as well. Figure 5.13,5.14,5.15 shows DCEP, DCEN, and AC square waves respectively.
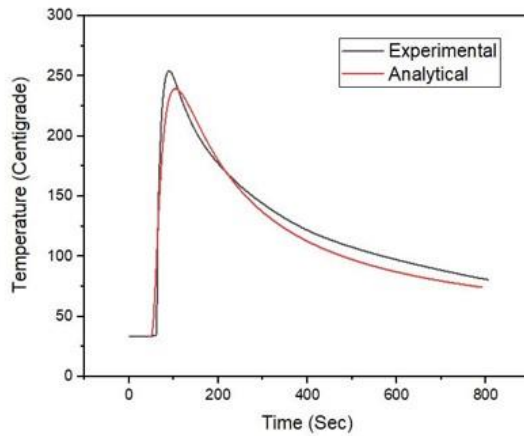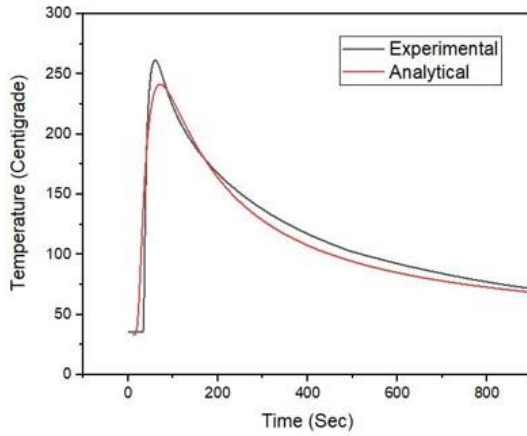

[Figure 5.13: DCEP surface mounted thermocouple]
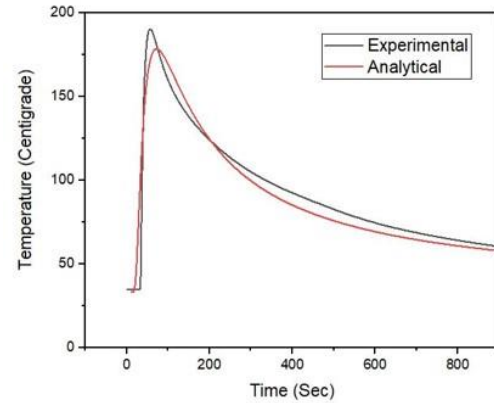
[Figure 5.14: DCEN surface mounted thermocouple]

A comparison between Analytical and numerical simulations for some experiments was estimated, and the results are displayed below, with Figures 5.16,5.17,5.18 representing a sample from DCEP, DCEN, and AC square waves respectively. An important inference can be made here, that though less accurate compared to the numerical analytical model is much more time saving and less resource-intensive, making it ideal for first degree estimates, as intended by this work.
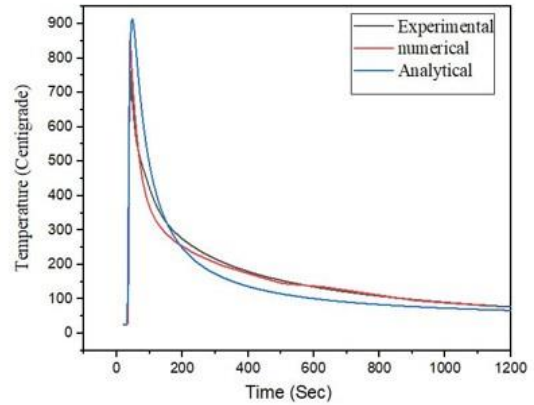
[Figure 5.15: AC square wave surface

mounted thermocouple]
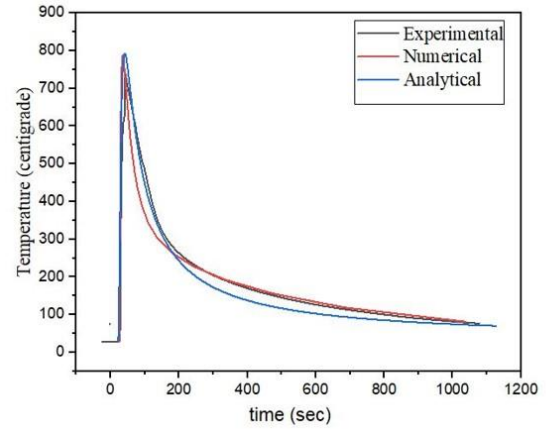
[Figure 5.16: DCEP experimental vs

numerical vs analytical]
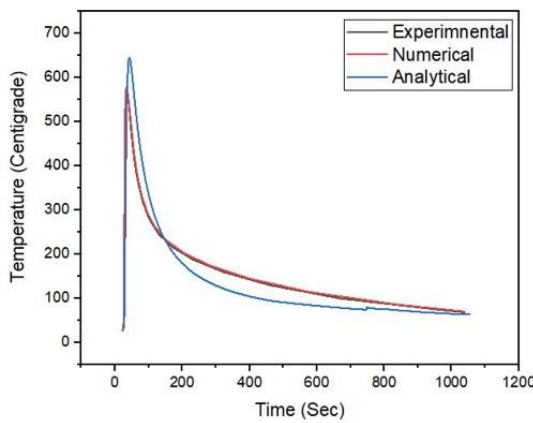
[Figure 5.17: DCEN experimental vs

numerical vs analytical]

[Figure 5.18: AC square wave

experimental vs numerical vs analytical]

5.2.6 Application: Intersection method

Once the model was stabilized with the displacement model, an application was

attempted, by replicating the work of John H Chujutalli et.al. In which a sample weld for

a parameter is done and the measured values are compared against a set of

predictions made by the analytical model, which is calculated over a range of input

parameters, and the intersecting parameters are considered to be ideal input

parameters to a numerical simulation, to simulate welds with the same settings, when

the numerical model uses same heat source model, in our case the Goldak double ellipsoidal heat source model.

Weld depth, width, and Peak temperature can be set as determinant values, for being the most convenient depth and width were used in the calculations performed. This model was utilized by another research team from IIT Tirupati and their observations are shown below with Figure 5.19 illustrating ah vs depth, 5.20 ah vs width, and 5.21 showing the intersection between the width and depth curves.
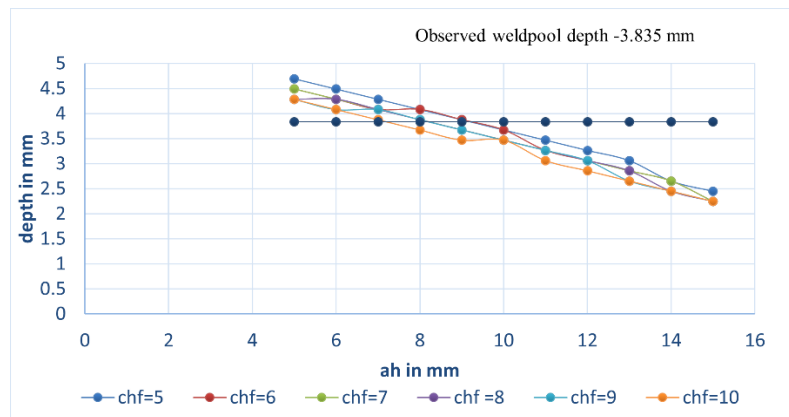
[Figure 5.19: ah vs depth]
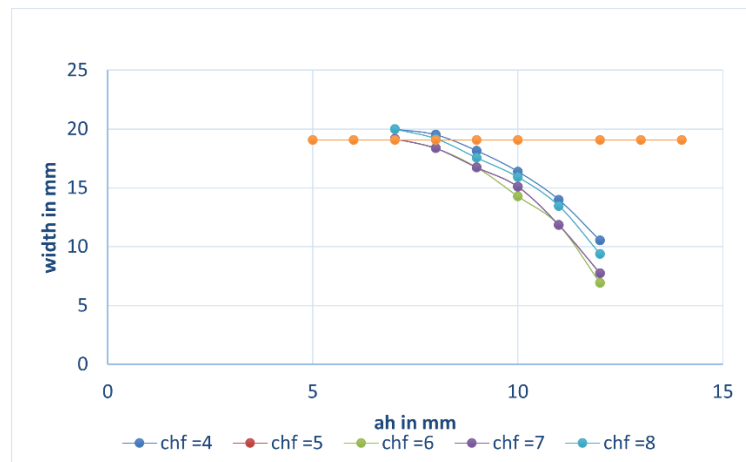

[Figure 5.20: ah vs width]
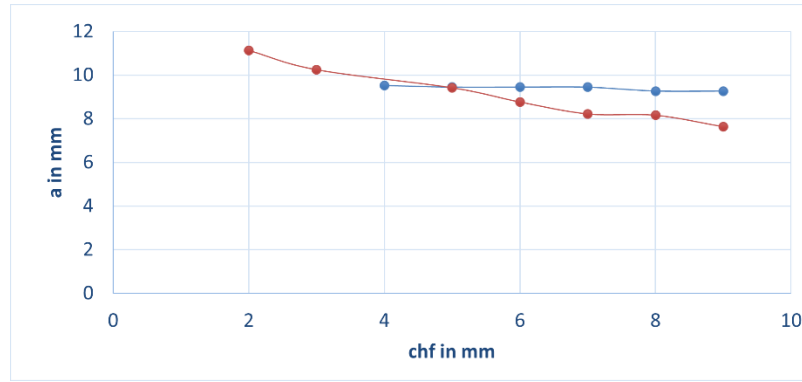
[Figure 5.21: ah vs depth]

The method provides a_h and c_{hf} and the rest of the parameters are estimated utilizing relations between them.

5.2.7 New Multi-pass thermal cycles

A multi-pass weld was performed to create a thin wall additively manufactured structure and the same experiment was simulated to validate the model's applicability in WAAM processes. Five thermocouple readings were taken while performing the weld and subsequently the conditions were simulated using the model. The results obtained show increasing deviation with an increase in the number of layers, But the results were still in an acceptable range. (Figures 22,23,24,25) Further experiments with a larger number of layers should be done to analyze complex and larger components.
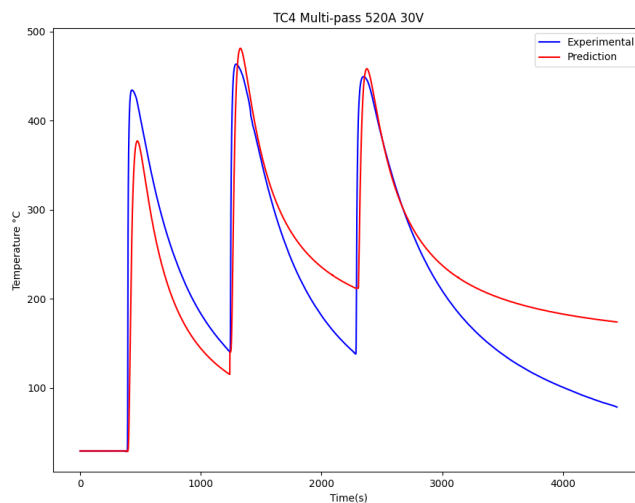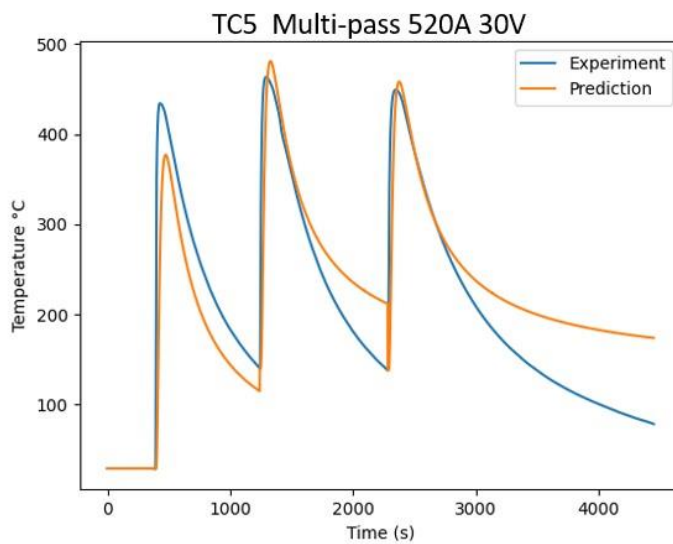
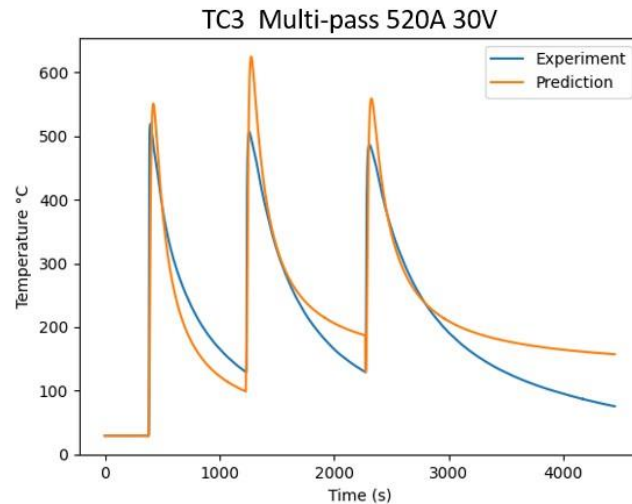[Figure 5.22: The multi-pass result from TC4 CV DCEP]
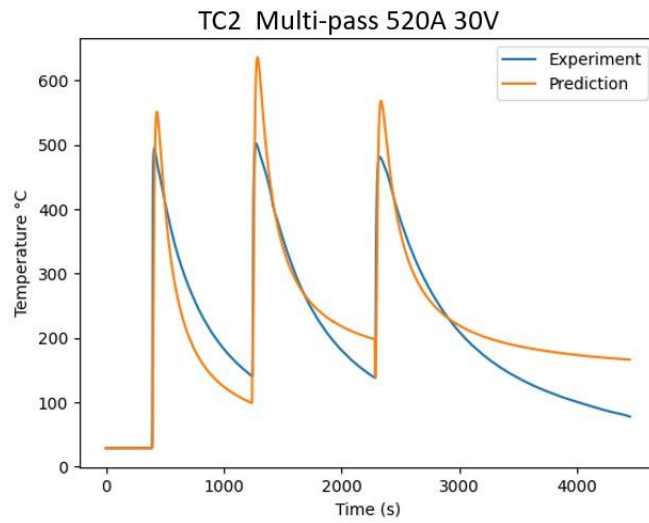
[Figure 5.23: The multi-pass result from TC2 CV DCEP]

Here the simulations are generated by cutting the heat source exactly as the experiments were timed, rather than waiting for the inter-pass temperature. This way the recreated results will be most representative of the real-world scenario.

[Figure 5.24: The multi-pass result from TC2 CV DCEP]

[Figure 5.25: The multi-pass result from TC2 CV DCEP]

5.2.8 Contour plots

Using the thermal field, through estimation of cooling rates, different metallurgical zones in the welded sample were estimated with the help of the model, as explained in section 4.6

CV Square wave at 410A and 30V was simulated and the result is shown below. Once the relevant parts of thermal cycles were calculated, peak temperature obtained by each point is compared with points in the Fe-C diagram, and categorized into sets, which is further utilized to generate a height map for the mesh grid created by the observation area linear spaces.
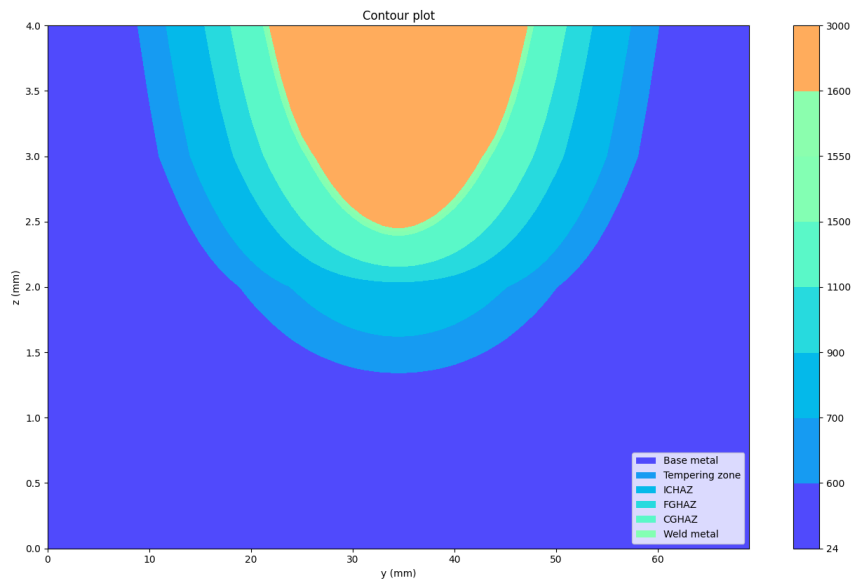
[Figure 5.26. CVSQ metallurgical contours simulated]

This functionality still needs to be improved however a primary stage implementation was successfully attempted. Due to the semi-infinite body approximation and lack of implementation of material deposition calculations, the bead height cannot be estimated from analytical contours like numerical ones. Nevertheless, a reliable prediction of the weld penetration and representation of heat affected zones (HAZ), are successfully estimated.

References:

1. J. Hu and H.-L. Tsai (2007). Heat and mass transfer in gas metal arc welding. part i: The ac. International journal of heat and mass transfer, 50(5-6), 833–846.

2. J. Ding, P. Colegrove, J. Mehnen, S. Ganguly, P. S. Almeida, F. Wang, and S. Williams (2011). Thermo-mechanical analysis of wire and arc additive layer manufacturing process on large multi-layer parts. Computational Materials Science, 50(12), 3315–3322.

3. Bai, Xingwang, et al. "Numerical analysis of heat transfer and fluid flow in multilayer deposition of PAW-based wire and arc additive manufacturing." International Journal of Heat and Mass Transfer 124 (2018): 504-516.

4. Cadiou, S., et al. "3D heat transfer, fluid flow and electromagnetic model for cold metal transfer wire arc additive manufacturing (Cmt-Waam)." Additive Manufacturing 36 (2020): 101541.

5. F. Montevecchi, G. Venturini, A. Scippa, and G. Campatelli (2016). Finite element modelling of wire-arc-additive-manufacturing process. Procedia Cirp, 55, 109–114.

6. Marcel Graf, A. Hälsig, K. Höfer, B. Awiszus, and P. Mayr (2018). Thermo-mechanical modelling of wire-arc additive manufacturing (waam) of semi-finished products. Metals, 8(12), 1009

7. Carslaw, H. S., and Jaeger, J. C. 1967. Conduction of Heat in Solids, Oxford University Press, Cambridge, U.K., pp. 255.

8. Goldak, John, Aditya Chakravarti, and Malcolm Bibby. "A new finite element model for welding heat sources." Metallurgical transactions B 15.2 (1984): 299-305.

9. Nguyen, Ninh & A, Ohta & K, Matsuoka & N, Suzuki & Y, Maeda. (1999).

Analytical Solutions for Transient Temperature of Semi-Infinite Body Subjected to 3-D Moving Heat Sources. Welding journal. August. 265s-274s.

10. Fassani, R. N. S., and O. V. Trevisan. "Analytical modeling of multipass welding process with distributed heat source." Journal of the Brazilian Society of Mechanical Sciences and Engineering 25.3 (2003): 302-305.

11. Reed, R. C., and H. K. D. H. Bhadeshia. "A simple model for multipass steel welds." Acta metallurgica et materialia 42.11 (1994): 3663-3678.

12. D. V. Kiran, J. Cheon, N. Arif, H. Chung, and S.-J. Na (2016). Three-dimensional finite element modeling of pulsed ac gas metal arc welding process. The International Journal of Advanced Manufacturing Technology, 86(5-8), 1453–1474.

13. V.D. Fachinotti, A.A. Anca, A. Cardona, Analytical solutions of the thermal feld induced by moving double ellipsoidal and double elliptical heat sources in a semi-infnite body. Int. J. Numer. Biomed. Eng. 27, 595–607 (2011)

14. Chujutalli, John & Lourenço, M.I. & Estefen, Segen. (2020). Experimental-based methodology for the double ellipsoidal heat source parameters in welding simulations. Marine Systems & Ocean Technology. 15.10.1007/s40868-020-00074-4.

15. Srivastava, Bipin & Tewari, Dr JYOTI, PRAKASH. (2010). A Review on Effect of Preheating and/or Post Weld Heat Treatmemt (Pwht) on Mechanical Behaviour of Ferrous Metals.. International Journal of Engineering Science and Technology.

16. L. O. Vilarinho and A. Scotti (2003), Proposal for a Modified Fowler-Milne Method to Determine the Temperature Profile in TIG Welding at Low Currents, COBEF 2003 – II Brazilian Manufacturing Congress.